Eidgenössische Technische Hochschule Zürich
Swiss Federal Institute of Technology Zurich

Simulating laser-ion interaction for quantum information processing

Master Thesis

Chloé Vernière

April 18, 2022

Supervisors: Alfredo Ricci Vasquez , Dr. Carmelo Mordini, Prof. Dr. Jonathan Home

TIQI Group, Dept. Phys., ETH Zürich

ETH

Eidgenössische Technische Hochschule Zürich
Swiss Federal Institute of Technology Zurich

Declaration of originality

The signed declaration of originality is a component of every semester paper, Bachelor's thesis, Master's thesis and any other degree paper undertaken during the course of studies, including the respective electronic versions.

Lecturers may also require a declaration of originality for other written papers compiled for their courses.

I hereby confirm that I am the sole author of the written work here enclosed and that I have compiled it in my own words. Parts excepted are corrections of form and content by the supervisor.

Title of work (in block letters):

Authored by (in block letters):
For papers written by groups the names of all authors are required.

Name(s): **First name(s):**

With my signature I confirm that
- I have committed none of the forms of plagiarism described in the 'Citation etiquette' information sheet.
- I have documented all methods, data and processes truthfully.
- I have not manipulated any data.
- I have mentioned all persons who were significant facilitators of the work.

I am aware that the work may be screened electronically for plagiarism.

Place, date **Signature(s)**

For papers written by groups the names of all authors are required. Their signatures collectively guarantee the entire content of the written paper.

Abstract

An ion trap with integrated photonics enables to generate phase-stable laser fields that can reliably adress one or many ions. It also gives the possibility to engineer specific light-fields that have rich interactions with the ions. In this thesis, I study the interaction of a Calcium ion in a surface-electrode Paul trap with a standing wave created by two counterpropagating laser beams at 729nm. This scheme provides position-dependent features in the Rabi frequencies of the $4S_{1/2} \rightarrow 3D_{5/2}$ electronic transitions and in the AC Stark shifts. The values of the Rabi frequencies oscillate with the standing-wave pattern and are show a spatial dephasing depending on the transition considered. Furthermore, the carrier and sideband Rabi frequencies for a given transition are spatially out-of-phase which allows to excite a sideband transition without off-resonantly driving the carrier one, while minimizing the AC Stark shift, which paves the way towards the implementation of high-fidelity two-ions Mølmer-Sørensen (MS) gates. Secondary goal of this thesis is to estimate how the temperature of the ion affects the values of Rabi frequencies we measure.

Acknowledgments

I would like to thank J. Home and D. Kienzler for giving me the opportunity to conduct my master thesis in the TIQI group. It was not only an opportunity to confront with state-of-the-edge reasearch, but also to learn a lot about experimental or theoritical hot topics and notions related to trapped ions and more genrally quantum physics.

None of the work I present here could have been done without the patient, always available and devoted to his work Alfredo Ricci Vasquez. I really enjoyed learning the ins and outs of the cryo set-up and delving deeper into the theory behind. I also thank Carmelo Mordini for his support and always apt suggestions and for letting me follow his struggles with the transport wavefunctions. I learnt a lot from you both and most of it cannot be written in this thesis.

Finally, I thank all the members of the TIQI group for garanteeing fruitful conversations and enjoyable time in the group and also the QSIT Network for granting me the QSIT Master Internship Award.

Contents

Chapter 1

Introduction

The evolution of computing performance predicted by Moore's law will come to a slowdown due to the extreme miniaturisation of electronic devices that would make them reach the quantum limit. In order to keep gaining computing power, research is performed towards building a quantum computer [1]. The latter uses *qubits* instead of bits as computing unit. A qubit being a superposition of two states, computing with them would allow to get important speed-up - as compared to their classical counterparts - on many computationnal taks, such as unstructured search in a list [2] or integer factorisation [3]. Quantum computing is fundamentally a different paradigm for computation. It takes advantage of the different ability of quantum systems to store and manipulate information and has thus intrinsic arguments to make regarding computing performance.

In the pursuit of building a quantum computer, several technologies to implement qubits are explored, from superconducting circuits [4] to Nitrogen vacancy centers in diamond [5] to name just a few. In this thesis, I will deal with one of the primary candidates, trapped ions [6, 7]. By engineering DC and RF electric fields, it is indeed possible to confine an ion spatially [8]. Encoding a qubit can then be done by using internal metastable or hyperfine energy levels of the valence electron or the ion's motional states [9]. In the first case, control of the encoded information is performed through the interaction of the valence electron with oscillating electric or magnetic fields. Choosing Calcium ions $^{40}Ca^{+}$ to work with seems a promising idea. Its electronic structure is diverse with dipole and quadrupole transitions between levels, the latter being long-lived, thus a good choice to define the qubit as they have long coherence time, whereas the first are short-lived, thus particularly adapted for state preparation, cooling and readout [7]. Possible coherence time is then greater than any gate time and primarily limited by classical control of the ion, with noisy lasers for instance.

The choice of the trap used to trap the ion is crucial. One could for instance use a Penning trap, which relies on static electric and magnetic fields, or a linear Paul trap, as it is the case in this thesis. This one relies only on static and oscillating electric fields to trap the ion. In such a trap, tens of ions can be trapped at the same time along the trap axis while still allowing single-ion adressing [10]. That is why this choice is a step towards scalability of trapped ion qubits. The choice of a surface Paul trap, where all the electrodes lie in the same plane, as opposed to a 3D trap, can be easily microfabricated and gives the possibility of photonics and control components integration below the surface [6]. Even if for the same applied voltages trapping potentials are less deep and trapping frequencies lower, which is often found to be detrimental to trapping, surface traps are nevertheless a promising technology for better integration and scaling. They are an important part of the technology explored for building quantum charge-coupled device in which ions are coupled or transported in different zones of the trap [11, 12] in order to build a universal quantum computer.

However, having a well-characterised and well-defined qubit also requires that it be isolated from the environment. For that, the trap is placed inside a vacuum chamber inside a cryostat, respectively for better trapping and minimisation of the electrical noise on the electrodes. In order to achieve even more stability, some of the light needed for the ion adressing is integrated into the trap, enhancing phase-stability and optical power efficiency while limiting cross-talk, paving the way for more simple and reliable mutli-ions adressing [13, 14, 15]. Furthermore, the integrated photonics can be used to create non-trivial light fields so as to give it interesting physical properties. In this thesis, two counterpropagating laser beams are emitted from the trap to the Calcium ion and forming a standing-wave along the trap axis. Importantly, the photonics and the trap are part of the same structure. It was hoped that this would provide good phase stability. This thesis provides work towards investigating whether this can be taken advantage of.

Working with ions in an optical lattice is not new, it has already been explored in the context of studying friction for instance [16, 17]. In our case, I will show that it can help reducing unavoidable computing errors when performing a two-qubits operation with a Mølmer-Sørensen gate [18], thus increasing the fidelity of the gate [19]. Following this idea, I study in this thesis the carrier and sideband Rabi frequencies and Stark shifts of three optical quadrupole transitions of a Calcium ion adressed by the standing-wave provided by the integrated photonics of a surface Paul trap.

This thesis is organised as follows. First, I will present the general interaction of a light field with an ion trapped in a surface Paul trap. Then, after describing the set-up, I will address the already-mentioned originality of the experiment, that is the standing wave laser-field and how it gives interesting properties to the ion. Lastly, I take a deeper look into the influence of temperature on the measurements of Rabi frequencies.

Chapter 2

Laser-ion interaction with trapped ions

In this Chapter, I present the general theory about ion trapping in a surface Paul trap and laser-ion interactions following [20, 21, 22].

2.1 What is an ion trap?

The trap used in the set-up is a surface-electrode Paul trap, composed of twenty electrodes that produce the electric fields which confines the ion.

2.1.1 Surface Paul trap

Let us first start with a description of a Paul trap, as a surface Paul trap is a planar version of it. One of the main challenges of trapping an ion in three dimensions is that Laplace's equation constraints a static potential to have a metastable saddle point. To overcome this issue, both static (DC) and time-varying (RF) electric potentials are used. A linear Paul trap [8] is thus constituted of four parallel rods to which DC and RF voltages are applied, thus creating a confining potential. The RF electrodes ensure radial (*id est* (*i.e.*) along the y and z axis) confinement, whereas the DC electrodes are responsible for the axial (*i.e.* along the x axis) confinement. The ion is then trapped in between those four electrodes, along their axis (see Figure 2.1, left panel). In a surface Paul trap, the 3D-geometry of the Paul trap is translated into a planar geometry: all electrodes are placed on the same plane, and the RF null, which defines the trapping axis, is located above the trap (see Figure 2.1, right panel). In our setup, ions are trapped at a distance $z = 50\mu$m above the surface of the trap. By applying different voltages on the DC electrodes, different potentials with different axial equilibrium positions are generated, thus allowing to control and vary the axial position of the ion.

Micromotion

More formally, with

$$\Phi_{RF}(\vec{r}, t) = 1/2(v_x x^2 + v_y y^2 + v_z z^2)\cos(\Omega_{RF} t + \phi)$$

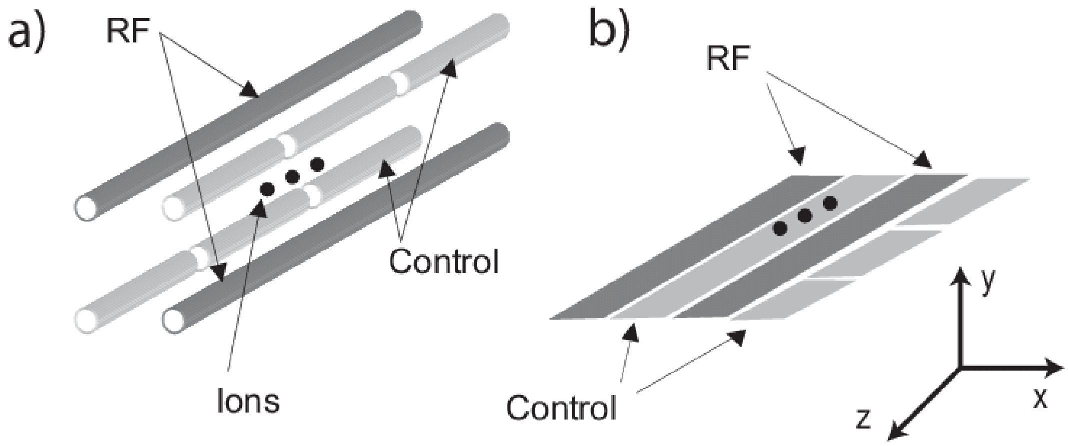

Figure 2.1: Linear Paul trap (*a*) and surface Paul trap (*b*), constituted of RF and DC electrodes[23]; ions are plotted along the RF null.

and

$$\Phi_{DC}(\vec{r}, t) = 1/2(u_x x^2 + u_y y^2 + u_z z^2),$$

respectively the RF and DC potentials, and two normalised variables $a_i = \frac{4eu_i}{m\Omega_{RF}^2}$ and $q_i = \frac{2ev_i}{m\Omega_{RF}^2}$ with m the mass of the ion, e the elementary charge, u_i and v_i constants that obey the Laplace equation and Ω_{RF} the RF modulation, the equations of motion are given by the Mathieu equation for $i = x, y, z$

$$\frac{d^2 r_i}{d\tau^2} + (a_i - 2q_i \cos(2\tau))\, r_i = 0 \tag{2.1}$$

with $\tau = \frac{\Omega_{RF} t}{2}$. In the limit $|a_i|$, $q_i^2 << 1$, for a confining linear Paul trap in the $y - z$ plane the motion follows

$$r_i \propto \cos\left(\frac{\beta_i}{2}\Omega_{RF} t\right)(1 + \frac{q_i}{2}\cos(\Omega_{RF} t)) \quad \text{for i} = y, z \tag{2.2}$$

$$r_x \propto \cos\left(\frac{\beta_i}{2}\Omega_{RF} t\right)$$

with $\beta_i = \sqrt{a_i + q_i^2/2}$.

Treating the ion as a three-dimensional harmonic oscillator, each of the modes of motion i oscillates with *secular* frequency $\frac{\beta_i}{2}\Omega_{RF}$. The second factor in radial Equation (2.2) denotes a modulation of the motion at the RF frequency, also known as micromotion. It can be neglected, unless the DC minimum is not in the RF null. This can happen for *intrinsic* factors, *i.e.* related to the trap configuration as for instance slight misalignement of the rods, or for *extrinsic* factors, that are usually stray fields.

2.2 Calcium ion

We trap Calcium ions $^{40}Ca^{+}$ as a means to store quantum information. By using lasers with precise control of their frequency, it is possible to control the single valence electron that evolves in the rich energy level structure of the ion showed in Figure 2.2, namely in the first energy levels available $4S_{1/2}$, $3D_{3/2}$, $3D_{5/2}$, $3P_{1/2}$ and $3P_{3/2}$. Here the levels are named following the standart atomic notation: nL_J with the total angular momentum $\vec{J} = \vec{L} + \vec{S}$. As in classical mechanics, any electron possesses an Orbital Angular Momentum (OAM) defined analogously as $\hat{L} = \hat{x} \times \hat{p}$. It also possesses a Spin Angular Momentum (SAM) $\vec{S}$. This quantity is conserved for a closed system. The total angular momentum quantum number j is defined such that $\hbar^2 j(j+1)$ is an eigenvalue of $\hat{J}^2$; m_j is the eigenvalue of $\hat{J}_z$, the projection of the total angular momentum $\hat{J}$ on the quantization axis. Those values are quantified. For an electron, the SAM is typically $1/2$, such that its projection on the quantisation axis can only be $\pm 1/2$ [24].

Internal state transitions are driven by applying an electric field at the transition's wavelength. We then encode an optical qubit in the Zeman sublevels $4S_{1/2}$ as $|0\rangle$ and $3D_{5/2}$ as $|1\rangle$. The degeneracy of those levels is lifted by the Zeeman effect when applying a magnetic field, creating fine-structure manifolds with equal spacing of $\Delta\omega = g_J \mu_B B/\hbar$ where g_J is the Landé g-factor, μ_B the Bohr magneton and B the magnetic field magnitude.

The transition involved in the optical qubit is an electric *quadrupole* transition excited by a 729nm laser: it is actually driven by the gradients of the electric field and shows small decay rates [21], which makes it well suited for a qubit. Another present electric quadrupole transition is $4S_{1/2}$ to $3D_{3/2}$, driven by a 732nm laser. Those transitions are denoted as *quadrupole*, since they are not dipole allowed, *i.e.* do not follow the dipole selection rules. They come from higher terms in the expansion of the Hamiltonian, use the spatial structure of the light to drive the transition and can exchange more than one quanta of angular momentum. On the contrary, all the other principal involved transitions at 393nm, 397nm, 854nm and 866nm are dipole transitions. These electric dipole transitions can be driven strongly even with low power, but have very short decay rates, they are for that reason not suited to store quantum information, but rather to perform state-preparation, cooling and readout via state-dependent fluorescence detection. During the latter process, the state is designated as *bright* if it is in the $|0\rangle$ state. The 397nm transition is driven, exciting the electron into the $3P_{1/2}$ level. From there, it decays back into $|0\rangle$, emitting a photon which can be subsequently captured by a photomultiplier tube. The detection of fluorescence photons indicates the $|0\rangle$ state. On the other hand, if the electron is in $|1\rangle$, it is not excited and the state remains *dark*: no photons are detected. However, during this process, a bright electron may as well decay into the $3D_{3/2}$ state. In order to detect it as bright, we need to drive the $3D_{3/2} \longrightarrow 3P_{1/2}$ transition using light at 866nm so as to repump the electron .

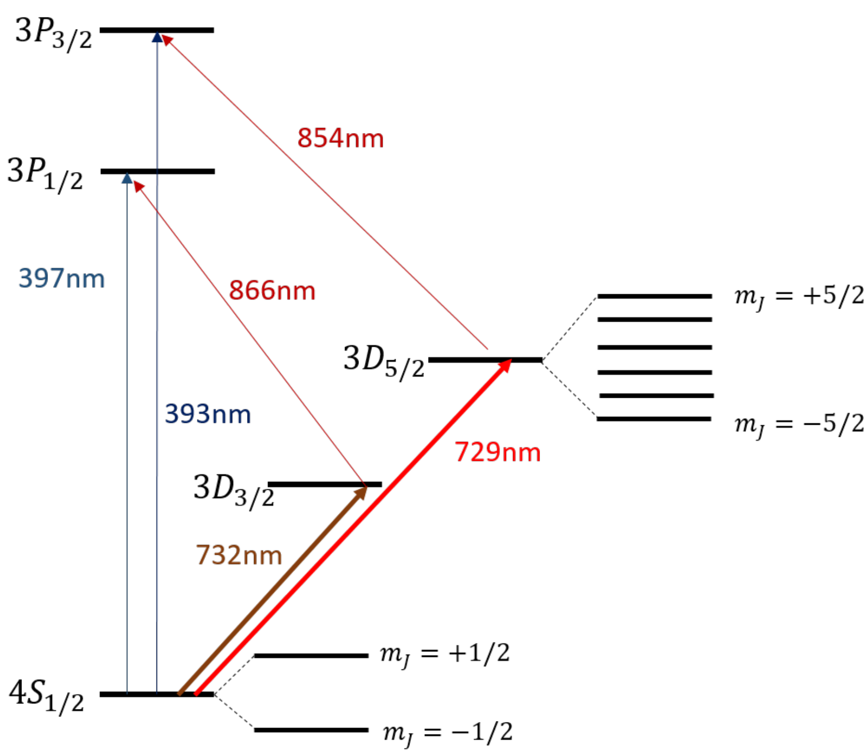

Figure 2.2: Calcium ion energy levels diagram with detailed Zeeman manifold on the $4S_{1/2}$ and $3D_{5/2}$ levels. Wavelengths of the transitions are indicated. Quadrupole transitions have *thick* lines, dipole transition *thin* lines.

2.3 Laser-ion interaction

We can derive a Hamiltonian that describes the interaction of a trapped ion qubit with a laser light [22]. For simplicity and as it captures most of the relevant phyiscs involved, let us study a two-level system with $|g\rangle$ and $|e\rangle$ the ground and excited state respectively. Let us start with its free Hamiltonian H_0 that describes the internal state level structure and the harmonic oscillator motional mode with

$$H_a = E_0 |g\rangle\langle g| + E_1 |e\rangle\langle e| =: \frac{\hbar\omega_o}{2}\sigma_z,$$

$$H_m = \hbar\omega_m \hat{a^\dagger}\hat{a}$$

and

$$H_0 = H_a + H_m$$

where $\sigma_z = |g\rangle\langle g| - |e\rangle\langle e|$, ω_o is the qubit transition frequency, ω_m is the frequency of the motional mode and $\hat{a^\dagger}$ (resp. $\hat{a}$) creation (resp. annilhilation) operators for this mode. I here consider only the axial mode of motion as the two radial ones will not be involved in this thesis.

The total Hamiltonian H also includes the interaction Hamiltonian H_I and reads

$$H = H_0 + H_I.$$

2.3.1 Rabi frequency

The interaction of the ion with the laser light can be treated using time-dependent perturbation theory. The formalism I use describes both electric dipole and quadrupole interactions to which a Rabi frequency Ω, a laser light frequency ω and a wavevector $\vec{k}$ can be associated. We can write the interaction Hamiltonian as [22]

$$H_I = \frac{\hbar}{2}\Omega\left(|e\rangle\langle g| + |g\rangle\langle e|\right)\left(e^{i(\vec{k}.\vec{R}-\omega t+\phi)} + e^{-i(\vec{k}.\vec{R}-\omega t+\phi)}\right) \tag{2.3}$$

where $\Omega = \frac{1}{\hbar}\langle e| H_I |g\rangle$ is called *Rabi frequency* of the interaction type involved and $\vec{R}$ is the position of the ion in the trap.

In the interaction picture with respect to H_0 and after applying the Rotating Wave Approximation (*i.e.* neglecting high frequency rotating terms), we obtain the Hamiltonian

$$H_I = \frac{\hbar}{2}\Omega\left(|e\rangle\langle g|\, e^{i(\vec{k}.\vec{R}-\delta t+\phi)} + |g\rangle\langle e|\, e^{-i(\vec{k}.\vec{R}-\delta t+\phi)} + \right) \tag{2.4}$$

where $\delta = \omega - \omega_o$.

For simplicity, let us first consider in the following paragraph that $\delta = 0$ and assume the position dependency as a constant phase such that $\phi = 0$. The time evolution is given by the unitary

$$U(t) = \exp(-iH_I t/\hbar) = \begin{pmatrix} \cos(\Omega t/2) & -i\sin(\Omega t/2) \\ i\sin(\Omega t/2) & \cos(\Omega t/2) \end{pmatrix}$$

which describes coherent oscilations between the $|g\rangle$ and $|e\rangle$ states at a frequency given by Ω. The probability to find the qubit in state $|e\rangle$ when it started in state $|g\rangle$ is given by $P_{|g\rangle}(|e\rangle, t) = \sin(\Omega t/2)^2 = \frac{1}{2}(1+\cos(\Omega t))$.

2.3.2 Sideband transitions

Let us now take a closer look into the motional part of the Hamiltonian (2.4). For simplicity, let us only consider only the axial motional mode ω_m. As the motion can modeled by an oscillator $\hat{x} = x_o(\hat{a}u^*(t) + \hat{a}^\dagger u(t))$ with $x_o = \sqrt{\frac{\hbar}{2m\omega_m}}$ the zero-point motion wavepacket and $u(t)$ solution to the Matthieu equation (2.1), the Hamiltonian must take into account the interaction of the light with this oscillator, which has both an amplitude and a direction.

We define the Lamb-Dicke parameter $\eta = k_x x_o = \frac{2\pi}{\lambda}\sqrt{\frac{\hbar}{2m\omega_m}}\cos(\theta)$, θ being the angle between the wavevector $\vec{k}$ and the x axis and λ the wavelength of the laser. In the Lamb Dicke regime, $\eta << 1$ and $\eta^2(n+1) << 1$ for $n \in \mathbb{N}$ the motional occupation number, this means that the light does not couple too strongly with the motion. This allows us to expand the exponential terms $e^{i\vec{k}\hat{R}} \approx 1 + i\eta(\hat{a}u^*(t) + \hat{a}^\dagger u(t))$. Writing $u(t)$ as a series in exponential and performing the RWA a second time yields

$$H_I = \frac{\hbar}{2}[\sum_n \Omega \left|e,n\right\rangle\!\left\langle g,n\right| e^{i(\delta t+\phi)} \\ + \sum_n i\sqrt{n+1}\eta\Omega \left|e,n+1\right\rangle\!\left\langle g,n\right| e^{i((\delta-\omega_m)t+\phi)} \\ + \sum_n i\sqrt{n}\eta\Omega \left|e,n\right\rangle\!\left\langle g,n+1\right| e^{i((\delta+\omega_m)t+\phi)}]. \quad (2.5)$$

The first sum is the analogous to the one in Equation (4.2) and describes the *carrier* Rabi frequency, obtained when resonantly driving the transition at $\delta = 0$. The second and third sums are the first sideband couplings obtained when driving the transition at $\delta = \pm\omega_m$.

Considering a single transition of the type $|g,n\rangle \leftrightarrow |e,n\rangle$,$|g,n\rangle \leftrightarrow |e,n+1\rangle$ and $|g,n+1\rangle \leftrightarrow |e,n\rangle$ respectively, we have for

- $\delta = 0$: $H_I = \frac{\hbar\Omega}{2}(\sigma_+ e^{i\phi} + \sigma_- e^{-i\phi})$ is the carrier Hamiltonian and Ω is the carrier Rabi frequency;
- $\delta = \omega_m$: $H_I = \frac{\hbar\eta\sqrt{n+1}\Omega}{2}(\sigma_+\hat{a}^\dagger e^{i\phi} + \sigma_-\hat{a}e^{-i\phi})$ is the blue sideband Hamiltonian and $\eta\sqrt{n+1}\Omega$ is the blue sideband Rabi frequency Ω_{bsb};
- $\delta = -\omega_m$: $H_I = \frac{\hbar\eta\sqrt{n}\Omega}{2}(\sigma_-\hat{a}^\dagger e^{-i\phi} + \sigma_+\hat{a}e^{i\phi})$ is the red sideband Hamiltonian and $\eta\sqrt{n}\Omega$ is the red sideband Rabi frequency Ω_{rsb}.

Here $\sigma_- = |g\rangle\langle e|$ and $\sigma_+ = |e\rangle\langle g|$ are the lowering and raising operators. The red (resp. blue) sideband interaction removes (resp. adds) a quanta of motion while exciting the ion. Since the coupling is reduced by the Lamb-Dicke parameter, one needs more power when driving a sideband transition as when driving a carrier transition to obtain the same coupling strength.

2.3.3 Stark shift

In the case of a detuned laser $\delta = \omega_L - \omega_0$, the total Hamiltonian in the RWA reads

$$H = \frac{\hbar\delta}{2}\sigma_z + \frac{\hbar}{2}\Omega \left|e\right\rangle\!\left\langle g\right| e^{-i(\delta t+\phi)} + \frac{\hbar}{2}\Omega \left|g\right\rangle\!\left\langle e\right| e^{i(\delta t+\phi)}. \quad (2.6)$$

When there is no detuning $\delta = 0$, the energy levels are exactly separated by $\hbar\omega_o$ as expected. However, supposing the detuning is larged compared to the Rabi frequency $\delta >> \Omega$, the eigenvalues of H are

$$E_\pm \approx \pm(\frac{\hbar\delta}{2} + \frac{\hbar\Omega^2}{4\delta}).$$

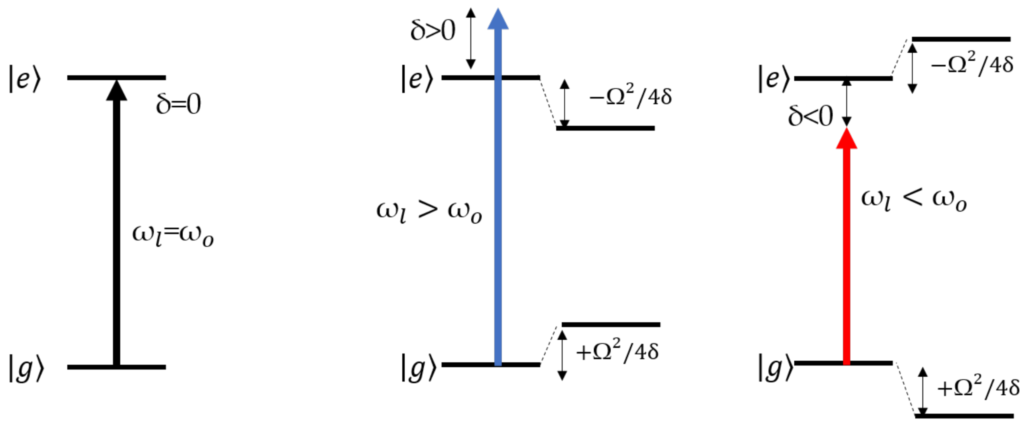

Figure 2.3: Driving a two level transition and AC Stark shift on the energy levels when $\delta >> \Omega$: resonantly (*left*), $\delta > 0$ (*center*) and $\delta < 0$ (*right*). A blue detuning (*center*) decreases the energy difference whereas a red detuning (*right*) increases it.

In this approximation, the first term reflects an energy shift between the qubit and drive frames and has thus no physical relevance. Whereas the second term has a physical interpretation and is known as the *AC Stark Shift*: when a transition is driven far from resonance, the energy levels are pushed apart or towards each other depending on the sign of the detuning, see Figure 2.3. This energy shift is of crucial importance for energy calibration and its applications in atomic clocks for instance.

For exhaustivity, if the laser is far detuned from the transition frequency, the counter rotating term known as the *Bloch-Siegert shift* must also be accounted for and contributes as $1/(\omega_L + \omega_0)$ in the total Stark shift calculation

$$\Delta E_{Starkshift} = -\frac{\hbar\Omega^2}{4}\left(\frac{1}{\omega_L - \omega_0} + \frac{1}{\omega_L + \omega_0}\right).$$

However, this contribution is still neglible in our case because $\omega_0, \omega_L >> |\omega_L - \omega_0|$.

Considering a more general case than the two-level system with a third level involved, this latter is also off-resonantly driven when we drive the qubit transition. For instance, in the case of the Calcium ion, driving the transition at 729nm actually off-resonantly drives all the other transitions, thus Stark shifting all the energy levels involved in those off-resonant transitions. This can be detrimental to the qubit frequency calibration as both initial and final states of the transition might be non negligeably shifted. This motivates the simulation and measurement of AC Stark shifts in Chapter 4.

Chapter 3

Experimental set-up

I now describe the experimental apparatus and techniques used to control and adress the qubit.

3.1 The set-up

The chip on which the trap is designed is located inside of a cryogenic chamber, which is itself inside a vacuum chamber. Temperature inside the cryogenic chamber is at 6K. Calcium neutral atoms come from the oven located on the side of the chamber. They are ionised in two steps [26]: first a 423nm laser drives the $4s^2\ ^1S_0 \rightarrow 4s4p\ ^1P_1$ atomic transition and we experimentally see neutral fluorescence. Then a 389nm laser removes the excited electron, the Doppler cooling and readout 397nm and 866nm lasers, that are always running, enable to cool and trap the ion and detect it once the

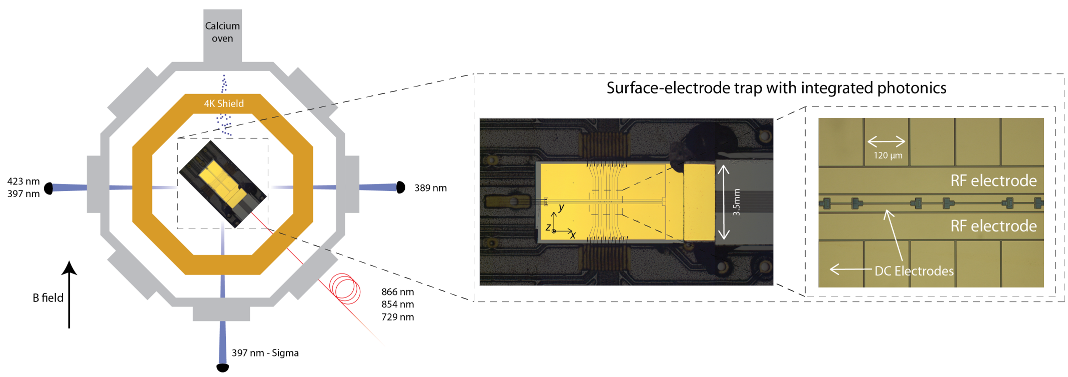

Figure 3.1: Scheme of the experimental set-up [25]. *Left*: vacuum chamber (*grey*), cryogenic chamber (*yellow*), Calcium oven in front of the top viewport, free-space laser lights (*blue*) through the three other viewports and integrated lights (*red*). The trap is in the center of the cryogenic chamber. *Center*: zoom on the surface electrode trap chip. *Right*: foccuss on the electrodes.

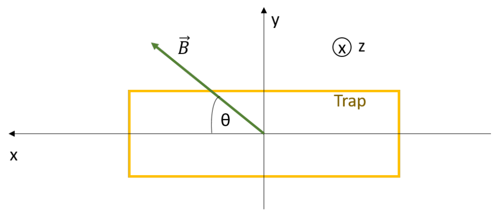

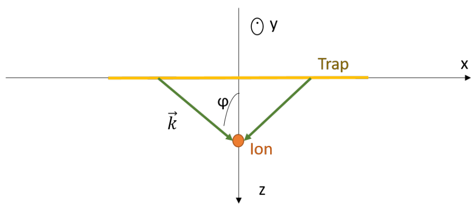

Figure 3.2: Geometric conventions. *Left*: view from above the trap (*yellow* rectangle) and orientation of the magnetic field in the trap frame. *Right*: lateral view, light emitted (*green*) by both couplers to the ion (*red*) beneath the trap chip (*yellow*).

atom is photoionized. In Figure 3.1, the left panel shows the vacuum chamber and cryostat disposition and how the light is delivered to the trap through the viewports. The right panel shows a zoomed-in picture of the trap. There are three zones of interest along the trap axis, each of them defined by the axial zone between two couplers. Out of the latter shine optical laser fields that allow to address ions reliably. The main interest of this set-up is the standing wave that is created by the 729nm counter-propagating laser beams coming out of these couplers.

During an experiment, the following lasers are used:

- a 389nm to photoionize the neutral Calcium ions;
- a 423nm laser also used to photoionize;
- a 397nm laser with σ polarisation to prepare the ion in the $|4S_{1/2}, m_j = -1/2\rangle$ state; one with π polarisation; those lasers are also used for EIT cooling and state-detection;
- a 729nm laser to adress the $4S_{1/2}$ to $3D_{5/2}$ transition, *ie* to address the qubit transition;
- a 854nm laser to repump the $3D_{5/2}$ state;
- a 866nm laser to repump the $3D_{3/2}$ state.

Out of those six different wavelength lasers, 389nm, 423nm and both 397nm polarisation ones are free-space whereas 729nm, 854nm and 866nm are integrated on the chip. This allows phase stability and ease of use, as they are less prone to fluctuations with time and in space [13].

The geometry of the set-up and conventions used are shown in 3.1. The trap lies in the $x-y$ plane, its axis being along x. The magnetic field lies in the same plane, it defines the quantisation axis and lifts the Zeeman sublevels. It makes a $\theta = 45°$ angle with the x axis (see Figure 3.2,left) and has a magnitude of approximatively 5.9G. Coming from the trap couplers, the 729nm laser light propagates along the z and x axis with an angle of $\phi = 36°$ with the trap normal (see Figure 3.2,right). In all experiments described in this thesis, a single ion is trapped $50\mu m$ away from the trap surface.

3.2 State preparation

At the beginning of each experiment, the electronic state is prepared in the $|4S_{1/2}, m_j = -1/2\rangle$ state. To do so, optical pumping on the dipole transition $4S_{1/2}$ to $3P_{1/2}$ is performed. It uses the fact that dipole transition selection rules depend on the polarisation of the laser light. For instance, adressing this transition with a 397nm σ polarised laser only allows to drive the $|4S_{1/2}, m_j = 1/2\rangle$ to $|3P_{1/2}, m_j = -1/2\rangle$ transition. From there, the electron can decay into $|4S_{1/2}, m_j = -1/2\rangle$. Thus, if we run this transition long enough, the electron get exponentially close to the $|4S_{1/2}, m_j = -1/2\rangle$ state, the main limitation being the polarization of the beam.

3.3 Measurement of the AC Stark shift

To measure the AC Stark shift on a transition, first a calibration of the qubit bare frequency is realised at low power. Then a pulse is applied at this frequency but high power, which results in shifting the energy levels due to the AC Stark shift caused by the off-resonant driving of the other transitions. This pulse is enclosed within two Ramsey $\pi/2$ pulse at the $4S_{1/2}$ to $3D_{5/2}$ transition frequency, such that the phase accumulated during this pulse is proportional to the energy shift. The Ramsey pulses allow to map this phase information into the population measurement at the end of the sequence. A series of pi-pulses with different lengths is then applied and yields a modulation of the measured population as a function of the length of the pulse with frequency equals to the differential Stark shift[27].

3.4 EIT Cooling

Electromagnetically-Induced Transparency (EIT) cooling allows to cool an ion below the Doppler limit by using a σ-polarised 397nm beam and a π-polarised one. Based on the three-level Λ system formed by the Zeeman sublevels of the $4S_{1/2}$ to $3P_{1/2}$ transition, the σ beam couples $|4S_{1/2}, m_j = -1/2\rangle$ to $|3P_{1/2}, m_j = 1/2\rangle$ and the π beam $|4S_{1/2}, m_j = 1/2\rangle$ to $|3P_{1/2}, m_j = 1/2\rangle$. The cooling rate R is then proportionnal to the projection of the difference of the 397nm wavevectors on the motional mode to cool with [28]

$$R \propto \left|(\vec{k}_\pi - \vec{k}_\sigma).\vec{e}_m\right|^2 \frac{\hbar}{2m\omega_m}$$

where $\vec{e}_m$ gives the direction of the oscillation.

During the process of my thesis, experiments were first done in the central zone of the trap, labelled zone 2. Then we moved to the zone on the right, zone 3. To be able to perform experiments in this second zone, most of the laser beams had to be moved towards it. If it is rather straightforward for the integrated lights, the non-integrated blue light had to be realigned in the new zone. When this was done, we realised that EIT cooling in that zone could not work as expected, as the difference of the σ-polarised and π-polarised laser wavevectors was aligned with the y axis rather than the x axis. It is then imposssible to cool the axial mode as it has no projection on

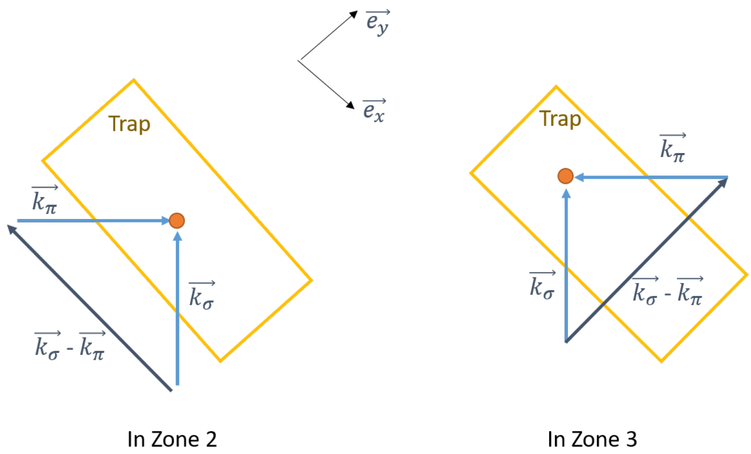

Figure 3.3: EIT cooling beams, 397nm σ- and π-polarised beams. The difference of their wavevectors in Zone 2 (*left*) and Zone 3 (*right*) is respectively along the x axis and y axis, allowing to cool the axial, resp. radial along y, mode only.

the wavevector difference. This discrepancy between the two zones is due to the fact that the σ beam was moved from one side of the trap to the other side when shifting from zone 2 to zone 3, thus modifying the difference of the wavevectors $\vec{k}_\sigma - \vec{k}_\pi$ (see Figure 3.3).

3.5 Protocol for running an experiment

When running an experiment, one has to make sure that the lasers cavities are optimally-detuned, that the polarisation of the 397nm σ- and π-laser beams is correct and that micromotion is well compensated. If we want to perform a Rabi flop measurement, the following steps are observed:

- initial state preparation;
- cooling;
- applying the 729nm pulse resonnant with one of the transitions during a given duration τ;
- reading out the state.

This procedure is repeated N times - usually N = 100 - to get statistics for this data point (see Figure 3.4). Before repeating it all over again to obtain the next data point of the plot.

Error on a data point

On each data point of an experiment, there is an error, a statistical uncertainty that can be quantified. The error ΔY on each data point is given by the quantum projection

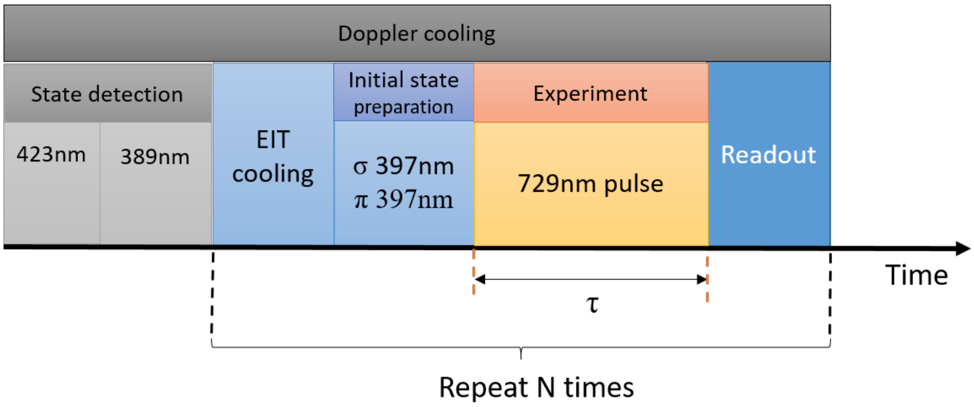

Figure 3.4: Scheme of an experimental protocol when running a Rabi flop. First the ion is loaded, while Doppler coolingand detecting it with 397nm laser. Then the state is prepared, a 729nm laser pulse of length τ is applied, before reading out the state. And these three last steps are repeated N times for statistics.

noise [29], defined as

$$\Delta Y = \sqrt{\max(\frac{Y(1-Y)}{N}, \frac{1}{N+2})}$$

where N is the number of measurements done to get one data point. The first term in this expression refers to a binomial distribution whereas the second term accounts for Y with values of 0 or 1 and comes from the Laplace rule (probability that the $(N+1)_{th}$ trial yields a different value when all the first N ones were equal).

Chapter 4

Study of Rabi oscillations in a standing wave

In this chapter, I study more precisely the ion interaction with the standing wave: firstly I derive the formula for the quadrupole, dipole and sideband Rabi frequencies, then for the *AC Stark shift*. Both Rabi frequencies and AC Stark shifts have noteworthy properties. In a second step, I study how variation in the magnetic field, polarisation or positioning of the couplers affect the Rabi frequencies. Finally, I consider the standing wave from the perspective of light with orbital angular momentum.

All the experiments were conducted between the $\left|4S_{1/2}, m_j = -1/2\right\rangle$ and the first sublevels of $|3D_{5/2}\rangle$ with $m_j = -5/2, -3/2$ or $-1/2$. Those three transitions capture distinct Δm_j that enable to cover all the behaviors provided by the standing wave. Then, considering the last two quadrupole allowed transitions to the $3D_{5/2}$ level with $\left|\Delta m_j\right| = 1$ and 2 is already redundancy, which allows us to confirm the other measurements of desired.

4.1 Working with a standing wave

The particularity of the set-up lies in the fact that the $729nm$ laser adressing the ion defines a phase-stable standing wave. From the two couplers, we have a standing wave along the trap axis x and a running wave along z

$$\vec{E}(\vec{r}, t) = E_0 \vec{\epsilon} \left(e^{i(k_z z - k_x x - \omega t)} + e^{i(k_z z + k_x x - \omega t)} \right),$$

$$\vec{E}(\vec{r}, t) = 2E_0 e^{ik_z z} \cos(k_x x - \omega t) \vec{\epsilon}.$$

The polarisation vector is $\vec{\epsilon} = \vec{e_y}$ and the wave vector propagates with an angle $\alpha = 36°$ to the vertical such that: $k_x = 2\pi/\lambda \sin(\alpha)$ and $k_z = 2\pi/\lambda \cos(\alpha)$.

In figure 4.1 is a finite-difference time-domain simulation of the actual electric field, provided by K. Mehta[1]. The beam is foccused at the trap center $(x, y) = (0, 0)$

[1]Former post-doctoral research assistant in the TIQI group.

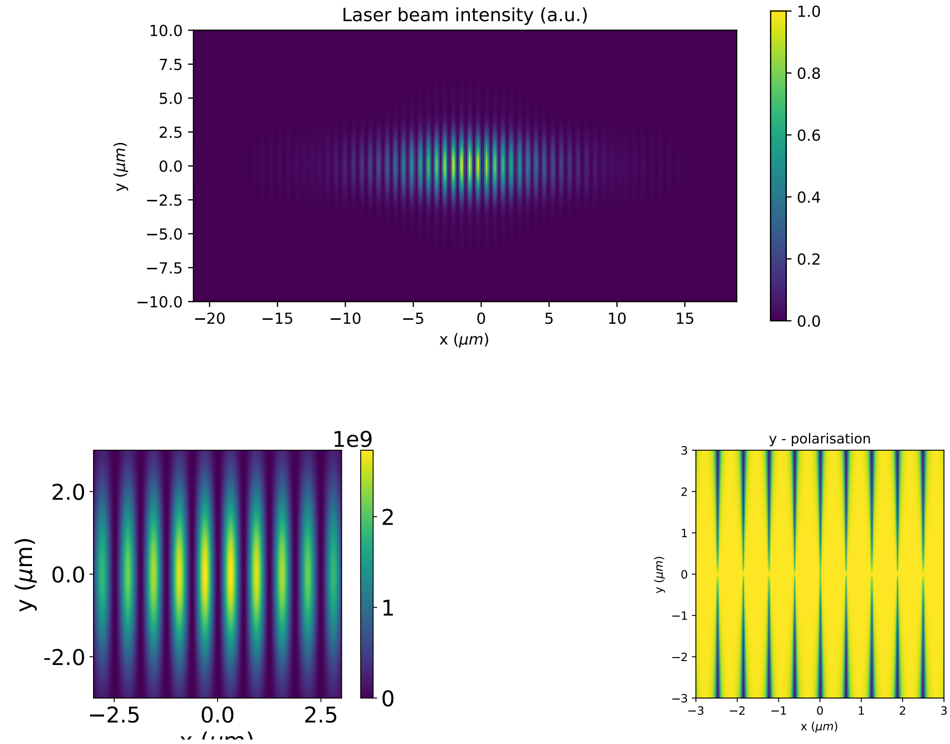

Figure 4.1: The standing wave (*top*) and a zoom in the center of the trap (*bottom left*). Purity of the y-polarization (*bottom right*). The intensity has here arbitrary values.

and the standing wave has a period of $729nm/\sin(36°) = 1.24\mu$m. If the ion remains on the trap axis, it experiences mainly a perfect y-polarisation of the field, whereas the farther away from the $y = 0$ axis, the more impure the polarisation is. The beam has the width at mid-height of 4.5μm along y and 11.7μm along x.

Conventions and basis

I will be using the following geometry (Figure 3.2): the trap axis defines the x-axis and its plane the $x - y$ plane; z is thus perpendicular to the trap plane. The magnetic fields, that lies in the $x - y$ plane, defines the quantisation axis. I will hence use the following matrix to rotate any vector that requires the quantisation axis to be parallel to z:

$$\mathcal{R} = \begin{pmatrix} -\sin(\theta) & -\sin(\phi)\cos(\theta) & \cos(\phi)\cos(\theta) \\ \cos(\theta) & \sin(\phi)\sin(\theta) & \cos(\phi)\sin(\theta) \\ 0 & \cos(\phi) & \sin(\phi) \end{pmatrix} \tag{4.1}$$

where θ is the angle between $\vec{B}$ and $\vec{e_x}$, ϕ between $\vec{B}$ and the $x - y$ plane.

As presented in [21], the interaction Hamiltonian given by the multipole expansion is

$$H_I = \frac{e}{2}\vec{E}.\vec{r} + \frac{e}{2}(\vec{r}.\vec{\epsilon})(\vec{\nabla}E_y.\vec{r}),$$

$$H_I = \frac{eE_o}{2}\vec{r}.\vec{\epsilon}e^{ik_z z}\cos(k_x x - \omega t) + \frac{eE_o}{2}(\vec{r}.\vec{\epsilon})(\vec{\nabla}(e^{ik_z z}\cos(k_x x - \omega t)).\vec{r}). \qquad (4.2)$$

Here $\vec{r}$ is the internal position of the electron and has to be distinguished from $\vec{R}$ the position of the ion in the trap. The first term of the sum in Equation (4.2) gives the dipole allowed interaction and the second term the quadrupole allowed interaction. I will first present the quadrupole Rabi frequency, as it is the one involved in the transition at 729nm.

From Equation (4.2), we can derive the quadrupole Rabi frequencies between a ground and excited states $|g\rangle$ and $|e\rangle$ respectively for the standing wave polarised along y starting from

$$\Omega^{qd} = \frac{e}{2\hbar}\left|\sum_i \langle e| r_i y |g\rangle \frac{\partial E_y}{\partial x_i}\right|. \qquad (4.3)$$

And the dipole Rabi frequency is analoguously given by

$$\Omega^{dp} = \frac{e}{2\hbar}\left|\langle e| y |g\rangle E_y\right|. \qquad (4.4)$$

I here use $x_i = x, y, z$ and E_j the projection of $\vec{E}$ on the x_j axis.

In the following, I note j, m_j the total angular momentum quantum numbers for the initial state $\left|4S_{1/2}, m_j = -1/2\right\rangle$ and j', m_j' for $\left|3D_{5/2}, m_j = -5/2, -3/2 \text{or} -1/2\right\rangle$ the final state .

4.1.1 Derivation of the quadrupole Rabi frequency

First, I expres the position operators r_i as a sum over regular spherical harmonics R_1^m $r_i = \sum_m c_i^{(m)} R_1^m$ (for details see Appendix A.1) with $(c^{(m)})_m$ the spherical unit vectors.

Then $r_i r_j = \frac{1}{3}r^2\delta_{i,j} + \sum_m c_{ij}^{(m)} R_2^m$, which is expressed with second rank spherical harmonics and

$$c_{ij}^{(q)} = \sqrt{\frac{10}{3}}(-1)^q \sum_{m_1,m_2=-1}^{1} \begin{pmatrix} j_0 & 2 & j_1 \\ m_0 & m_1 & -q \end{pmatrix} c_i^{(m_1)}.c_j^{(m_2)}$$

where $\begin{pmatrix} \mathrm{j}_0 & 2 & \mathrm{j}_1 \\ \mathrm{m}_0 & \mathrm{m}_1 & -q \end{pmatrix}$ is the Wigner-3j symbol. With this expression, we get

$$\langle e| r_i r_j |g\rangle = \sum_{m=-2}^{2} \langle e| R_2^m |g\rangle c_{ij}^{(2)}.$$

Since our magnetic field is not along the direction of progation of the light, we need to rotate the $c_{ij}^{(q)}$ so as to match our quantisation axis. From now on, $c_{ij}^{(q)}$ is defined as $(\mathcal{R}c^{(q)}\mathcal{R}^{-1})_{ij}$ with $\mathcal{R}$ from (4.1). Appling the Wigner-Eckart theorem (see Appendix A.1.1), we get

$$\langle e|\, r_i r_j \,|g\rangle = \langle e|\,|R^2|\,|g\rangle \sum_{q=-2}^{2} \begin{pmatrix} j & 2 & j' \\ -m_j & q & m_j' \end{pmatrix} c_{ij}^{(q)}.$$

We can relate $\langle e|\,|R^{(2)}|\,|g\rangle$ to the Einstein coefficent (Appendix A.3) of the transition involved with

$$A_{12}^{(E_2)} = \frac{c\alpha k_{12}^5}{15(2j'+1)} |\,\langle e|\,|R^{(2)}|\,|g\rangle\,|^2.$$

Finally

$$\Omega^{qd} = \frac{1}{2\hbar}\sqrt{\frac{15(2j'+1)}{c\alpha}}\sqrt{\frac{A_{12}^{(E_2)}}{k_{12}^5}}\left|\sum_{q=-2}^{2} \begin{pmatrix} j & 2 & j' \\ -m_j & q & m_j' \end{pmatrix} \sum_{ij} c_{ij}^{(q)} \frac{\partial E_i}{\partial x_j}\right|. \tag{4.5}$$

In particular, for the $\left|4S_{1/2}, m_j = -1/2\right\rangle \to \left|3D_{5/2}, m_j'\right\rangle$ transition, with our standing wave and writing $C^2_{j=5/2,k} = \frac{1}{2\hbar}\sqrt{\frac{15(2\frac{5}{2}+1)}{c\alpha}}\sqrt{\frac{A_{12}^{(E_2)}}{k_{12}^5}}$

$$\Omega^{qd} = C^2_{j=5/2,k}\left|\sum_{q=-2}^{2} \begin{pmatrix} 1/2 & 2 & 5/2 \\ 1/2 & q & m_j' \end{pmatrix} \left(-c_{yx}^{(q)} E_0 e^{ik_z z} k_x \sin k_x x + c_{yz}^{(q)} ik_z E_0 e^{ik_z z} \cos k_x x\right)\right|. \tag{4.6}$$

We clearly see in Equation (4.5) why quadrupole transitions only allows $|\Delta m_j| = 2, 1$ or 0 and $|\Delta j| = 2, 1$ or 0: the Wigner-3j symbol is zero if one of these conditions is not satisfied. For example, the $\left|4S_{1/2}, m_j = -1/2\right\rangle$ state can never couple to the $\left|3D_{5/2}, m_j = 5/2\right\rangle$ state.

Equation (4.6) already tells us a lot about the influence of the standing wave pattern on the quadrupole Rabi frequencies for this transition. Let us first factor out $e^{ik_z z}$ as a global phase since the position along z is fixed at 50μm and rewrite it in a more compact and insightful way

$$\Omega^{qd} = \left|E_0(\langle e|\, r_y r_x \,|g\rangle, 0, \langle e|\, r_y r_z \,|g\rangle).(-k_x \sin k_x x, 0, ik_z \cos k_x x)\right|.$$

If the ion sits at a node of the standing wave where $\cos k_x x = 0$, then the only remaining term in this expression is due to the gradient along x of the electric field. In particular, if $\langle e|\, r_y r_x \,|g\rangle$ is non zero, then the transition is driven where there is actually no field intensity ! This might be a bit puzzling at first sight, but what drives a quadrupole transition is the gradient of the electric field, which allows this particularity. On the contrary, if the ion sits at an anti-node of the standing wave where $\cos k_x x = 1$, then the transition is driven by the gradients along z of the electric field, *i.e.* by the running wave along z.

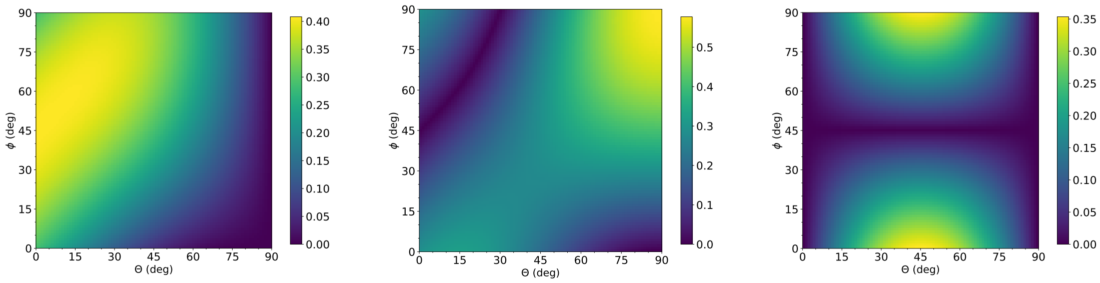

Figure 4.2: Coupling as a function of the magnetic field angles θ and ϕ for $\left|\Delta m_j\right| = 2$ (*left*), $\left|\Delta m_j\right| = 1$ (*center*) and $\Delta\ m_j = 0$ (*right*)

Couplings

The geometry has also an influence on how strongly a transition can be driven. Let us consider the coupling strength, defined as

$$g(\Delta m, \theta, \phi) = | - c_{yx}^{(\Delta m)} \sin\theta + c_{yz}^{(\Delta m)} i \cos\theta|$$

where $c_{i,j}$ depends on ϕ as it is rotated to match the quantisation axis defined by $\vec{B}$. As presented in 4.2, there are couples of angles (θ, ϕ) that are particurly favorable to drive a given transition or more interestingly not to drive a transition: for instance setting the magnetic field parallel to the y axis, *i.e.* $\theta = 90°$, prevents driving any transition with $\left|\Delta m_j\right| = 2$ or 0, and so for any orientation of the wavevector. We however choose the magnetic field so as to be able to drive all three transitions, hence the choice of $\theta = 45°$ and $\phi = 0$.

4.1.2 Derivation of the dipole Rabi frequency

I here derive the dipole Rabi frequency because it is relevant to evaluate the Stark shift. The derivation follows the same pattern as for the quadrupole Rabi frequency, the main difference being the presence of first rank tensors instead of second rank tensors

$$\Omega^{dp} = \frac{e}{2\hbar} \left| \sum_i \langle e| \, |R^1| \, |g\rangle \sum_{q=-1}^{1} \begin{pmatrix} j & 1 & j' \\ -m_j & q & m'_j \end{pmatrix} c_i^{(q)} E_i \right|.$$

Using the expression for the Einstein A cefficients (Appendix A.3), we finally get

$$\Omega^{dp} = \frac{1}{2\hbar} \sqrt{\frac{3(2j'+1)}{c\alpha}} \sqrt{\frac{A_{12}^{(E_1)}}{k_{12}^3}} \left| \sum_{q=-1}^{1} \begin{pmatrix} j & 1 & j' \\ -m_j & q & m'_j \end{pmatrix} \sum_i c_i^{(q)} E_i \right|.$$

With our standing wave, writing $C^1_{j',k} = \frac{1}{2\hbar}\sqrt{\frac{3(2j'+1)}{c\alpha}}\sqrt{\frac{A^{(E_1)}_{12}}{k^3_{12}}}$, the dipole Rabi frequency is

$$\Omega^{dp} = C^1_{5/2,k}\left|\sum_{q=-1}^{1}\begin{pmatrix} j & 1 & j' \\ -m_j & q & m'_j \end{pmatrix}\sum_i c_y^{(q)} E_0 e^{ik_z z}\cos(k_x x)\right|.$$

Here again, the Wigner-3j symbol only allows transitions between states with $|\Delta m_j| = 1$ or 0 and $|\Delta j| = 1$ or 0. The dipole Rabi frequency is driven by the electric field and directly proportionnal to its amplitude. Thus if the ion sits at a node, no transition can be driven.

4.1.3 Derivation of the sideband Rabi frequency

We assume we are in the Lamb-Dicke regime and hence can Taylor expand terms with $k_x\hat{x} = k_x\hat{x_o} + \eta(\hat{a} + \hat{a}^\dagger)$ where x_o is the position of the ion, η the Lamb-Dicke parameter, and get

$$\sin k_x x \approx \sin(k_x x_o) + \eta(\hat{a} + \hat{a}^\dagger)\cos(k_x x_o)$$

and

$$\cos k_x x \approx \cos(k_x x_o) - \eta(\hat{a} + \hat{a}^\dagger)\sin(k_x x_o).$$

Performing the RWA, we finally obtain

$$\Omega^{qd}_{sb} = C_{J=5/2,k}E_0\eta\left|\sum_{q=-2}^{2}\begin{pmatrix} 1/2 & 2 & 5/2 \\ 1/2 & q & m'_j \end{pmatrix}\left(-c^{(q)}_{yx}k_x\cos k_x x_o - c^{(q)}_{yz} ik_z \sin k_x x_o\right)\right|.$$

Here we are actually applying Equation(4.6) to $\frac{\partial E}{\partial x}$. Rewriting it more compactfully

$$\Omega^{qd}_{sb} = \eta E_0\left|\left(\langle e|\, r_y r_x\, |g\rangle, 0, \langle e|\, r_y r_z\, |g\rangle\right).(-k_x\cos k_x x, 0, -ik_z\sin k_x x)\right|.$$

4.1.4 Results

In figure 4.3 I present the Rabi frequencies of the transitions$\left|4S_{1/2}, m_j = -1/2\right\rangle$ to $\left|3D_{5/2}, m'_j = -5/2; -3/2 \text{ and } -1/2\right\rangle$ as a function of position along the trap axis. The plain lines are computed with a full numerical model of the field in the trap -that I will call *real*- whereas the dashed ones are computed with an interfering plane wave model. We can indeed see that away from the trap center $(x, y) = (0, 0)$ the amplitude of the *real* Rabi frequencies is reduced compared to the *ideal* ones: this due to the fact that the laser light has a beam shape foccussed at the trap center. We also see a first interesting feature here: the three transitions do not have the same phase along the trap axis. In particular, when driving the transition to $\left|3D_{5/2}, m'_j = -1/2\right\rangle$ at a position where its Rabi frequency is maximum, the Rabi frequency of the transition to $\left|3D_{5/2}, m'_j = -3/2\right\rangle$ is minimum if not zero. That means that we are not driving off-resonantly this transition. The transition to $\left|3D_{5/2}, m_j' = -5/2\right\rangle$, even more off-resonant, is also not fully driven. This standing wave pattern allows to select which transition is driven while not driving off-resonantly the other ones of the Zeeman manifold by choice of ion position. This could also be realised by increasing the magnetic field value or changing the quantization angle such that some transitions cannot be driven, it is thus not the preserve of the standing wave pattern. For instance, let us suppose the ion is exactly in the center of the trap, where the transition to $\left|3D_{5/2}, m_j' = -1/2\right\rangle$ Rabi frequency is maximum and the one to $\left|3D_{5/2}, m_j' = -3/2\right\rangle$ zero. At this position, the transition to $\left|3D_{5/2}, m_j' = -5/2\right\rangle$ Rabi frequency is approximately half of the one of the one to $\left|3D_{5/2}, m_j' = -1/2\right\rangle$. To get a coupling of the same magnitude, without even taking the detuning into account, one would need four times more intensity.

As for the sideband Rabi frequencies, they show the same properties. Nevertheless, since they are calculated with the axial gradient of the gradient of the carrier Rabi frequency, they have exactly a $\pi/2$ phase-shift with their carrier counterparts. That is to say, when the carrier Rabi frequency is maximum for a transition, the sideband Rabi frequency is minimum, *i.e.* zero, and vice-versa. This is of crucial importance and benefit for quantum information processing. As derived in [18], one important error when performing a Mølmer-Sørensen gate scales quadratically with the carier Rabi frequency when this off-resonant coupling is taken into account. The fidelity is then given by

$$F = 1 - \frac{\Omega_c^2}{\delta^2}(1 - \cos(2\delta\tau))$$

where $\tau = \frac{\pi}{\Omega_{sideband}}$ is the gate time, usually fixed, and δ the detuning used to drive the gate. Implementing such a gate in the standing wave would not only allow to drive the gate at maximum power, *i.e.* maximum sideband Rabi frequency and minimum gate time, but also to minimize the error by cancelling the carrier Rabi frequency.

4.1.5 AC Stark shift

Stark shift for the carrier transition

When resonantly driving any $|4S_{1/2}, m_j = -1/2\rangle$ to $\left|3D_{5/2}, m_j'\right\rangle$ transition, any other atomic transition is *de facto* off-resonantly driven. All the off-resonantly driven transitions in which any of those two levels are involved is thus affected by the *AC Stark shift*. It is evaluated as the shift in the energy difference of the two levels

$$\Delta E = \text{"shift on the } 3D_{5/2} \text{ level" - "shift on the } 4S_{1/2} \text{ level"}.$$

On the $3D_{5/2}$ level, there is a contribution from the $3P_{3/2}$ to $3D_{5/2}$ transition at 866nm and a contribution from $4S_{1/2}$, $m_j = +1/2$. On $4S_{1/2}$ level, there are contributions from the off-resonantly driven dipole allowed transitions at 397nm and 393nm to $3P_{1/2}$ and $3P_{3/2}$ respectively; and finally from the off-resonantly driven

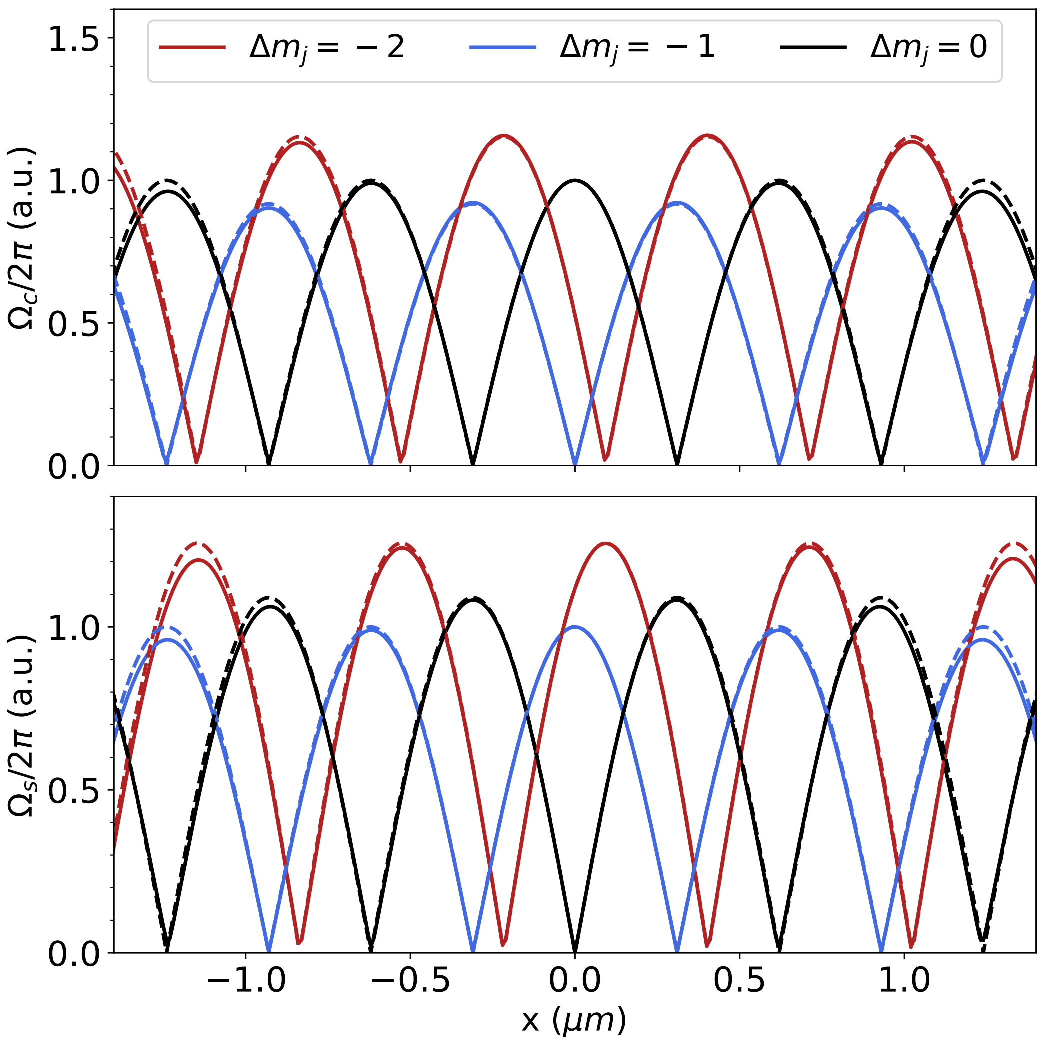

Figure 4.3: Carrier (*top*) and sideband (*bottom*) Rabi frequencies for the simulated field (*full*) and plane wave model (*dashed*) of the three transitions considered. Values are normalized to the value of the $\Delta m_j = 0$ (resp. $\Delta m_j = 1$) transition at $x = 0$ for the carrier (resp. sideband).

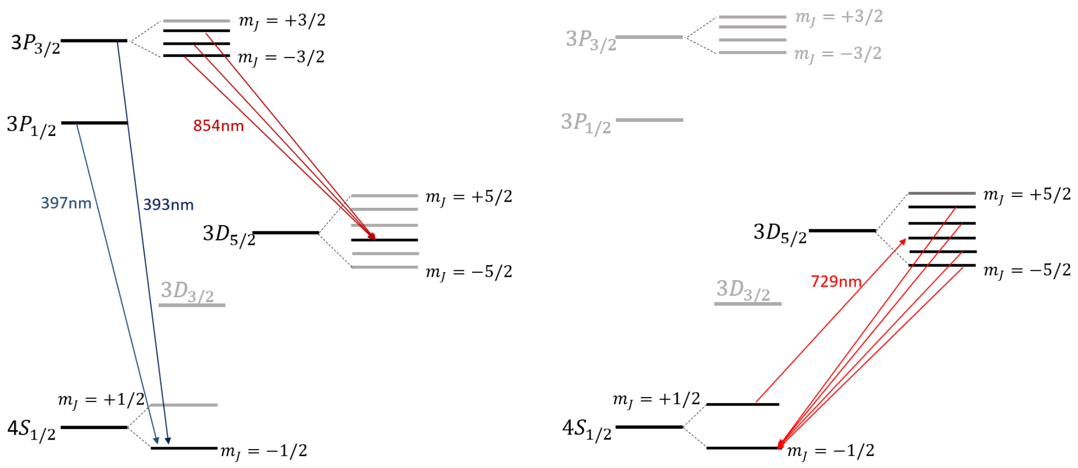

Figure 4.4: Dipole (*left*) and quadrupole (*right*) transitions involved in the calculation of the total AC Stark shift when driving the transition between $|4S_{1/2}, m_j = -1/2\rangle$ to $|3D_{5/2}, m_j = -1/2\rangle$.

quadrupole transition at 729nm in the $3D_{5/2}$ Zeeman manifold.

$$\Delta E \quad = \quad \frac{\hbar}{4}\left[\frac{\Omega_{854}^2}{\delta_{854}} + \frac{\Omega_{729,+1/2}^2}{\delta_{729,+1/2}} - \left(-\frac{\Omega_{393}^2}{\delta_{393}} - \frac{\Omega_{397}^2}{\delta_{397}} - \frac{\Omega_{729,-1/2}^2}{\delta_{729,-1/2}}\right)\right] \tag{4.7}$$

where δ_λ is the detuning between the driving laser at 729nm and the off-resonantly driven transition at λnm, Ω_λ the Rabi frequency of the transition at λnm. The subscript $729, +1/2$ (resp. $729, -1/2$) refers to the $|4S_{1/2}, m_j = +1/2\rangle$ (resp. $|4S_{1/2}, m_j = 1/2\rangle$) associated detuning and Rabi frequency. In Figure 4.4 I have decomposed the effect of the off-resonantly driven transitions depending if they are dipole or quadrupole allowed.

We neglect other transitions that could contribute as well as any contribution from sideband Rabi frequencies, as they are about 10 to 100 times smaller for a similar detuning due to lower Rabi frequencies.

In Figure 4.5 the main contribution to the Stark shift comes from the off-resonantly driven dipole transitions. The contributions from the quadrupole transitions are by one order of magnitude smaller and depend more strongly on which transition is driven. They cause the total AC Stark shift to be different depending on which transition is driven.

Stark shift when driving a sideband transition

Now let us suppose we drive a blue-sideband of the transition $|4S_{1/2}, m_j = -1/2\rangle$ to $|3D_{5/2}, m_j = -5/2\rangle$. The total Stark shift can be derived as previously, updating the detunings since we are 1.6MHz bluer and also taking into account the contribution from the closest carrier transition. The latter contributes twice, since both energy

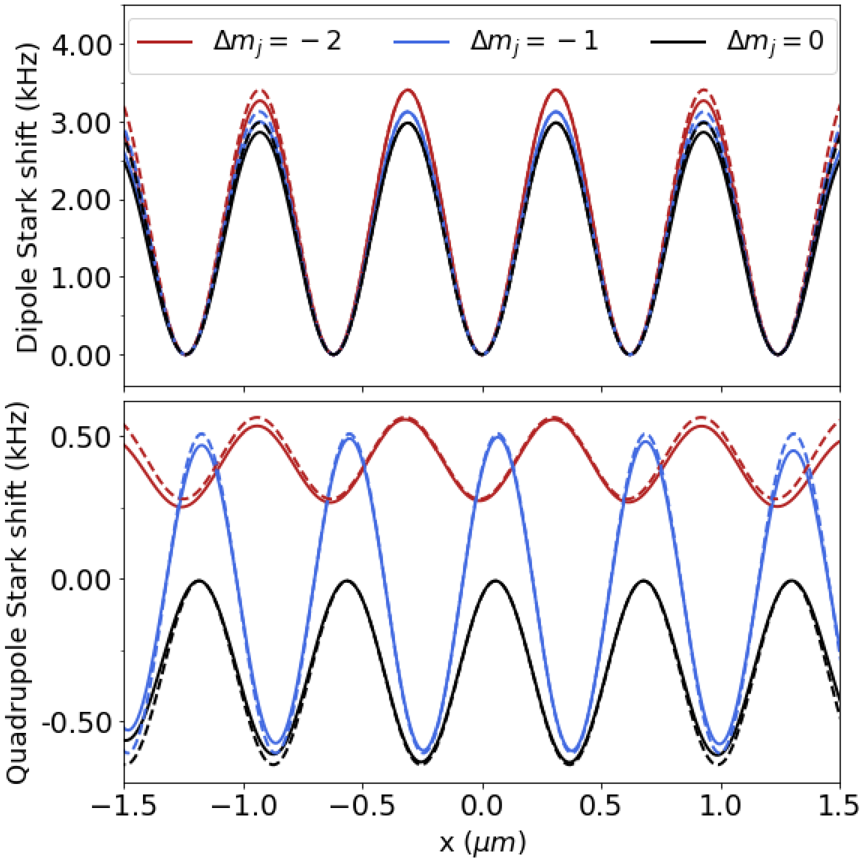

Figure 4.5: Dipole and quadrupole transitions contributions to the AC Stark shift (full: simulated field; dashed: plane wave model).

levels are involved in the measurement of the AC Stark shift. We finally get:

$$\Delta E = \frac{\hbar}{4}\left[\frac{\Omega_{866}^2}{\delta_{866}} + \frac{\Omega_{729}^2}{\delta_{729,+1/2}} + \frac{\Omega_{729,-1/2,c}^2}{-w_m} - \left(-\frac{\Omega_{393}^2}{\delta_{393}} - \frac{\Omega_{397}^2}{\delta_{397}} - \frac{\Omega_{729,-1/2}^2}{\delta_{729,-1/2}} - \frac{\Omega_{729,-1/2,c}^2}{-w_m}\right)\right]. \tag{4.8}$$

Here the detunings also take into account the fact that the drive is ω_m bluer and $\Omega_{729,-1/2,c}$ refers to the carier whose sideband is driven. The main contribution, on top of the dipole ones, comes precisely from this carrier transition since it driven close to resonance, such that the main difference with the carier Stark shift comes from the $\frac{\Omega_{729,-1/2,c}^2}{-w_m} - (-\frac{\Omega_{729,-1/2,c}^2}{-w_m}) = -2\frac{\Omega_{729,-1/2,c}^2}{w_m}$ supplementary term.

4.1.6 Results

In Figure 4.6 are regrouped all the results from the calculations. On top of the already pointed out interesting features such as the $\pi/2$ phase shifts between carrier

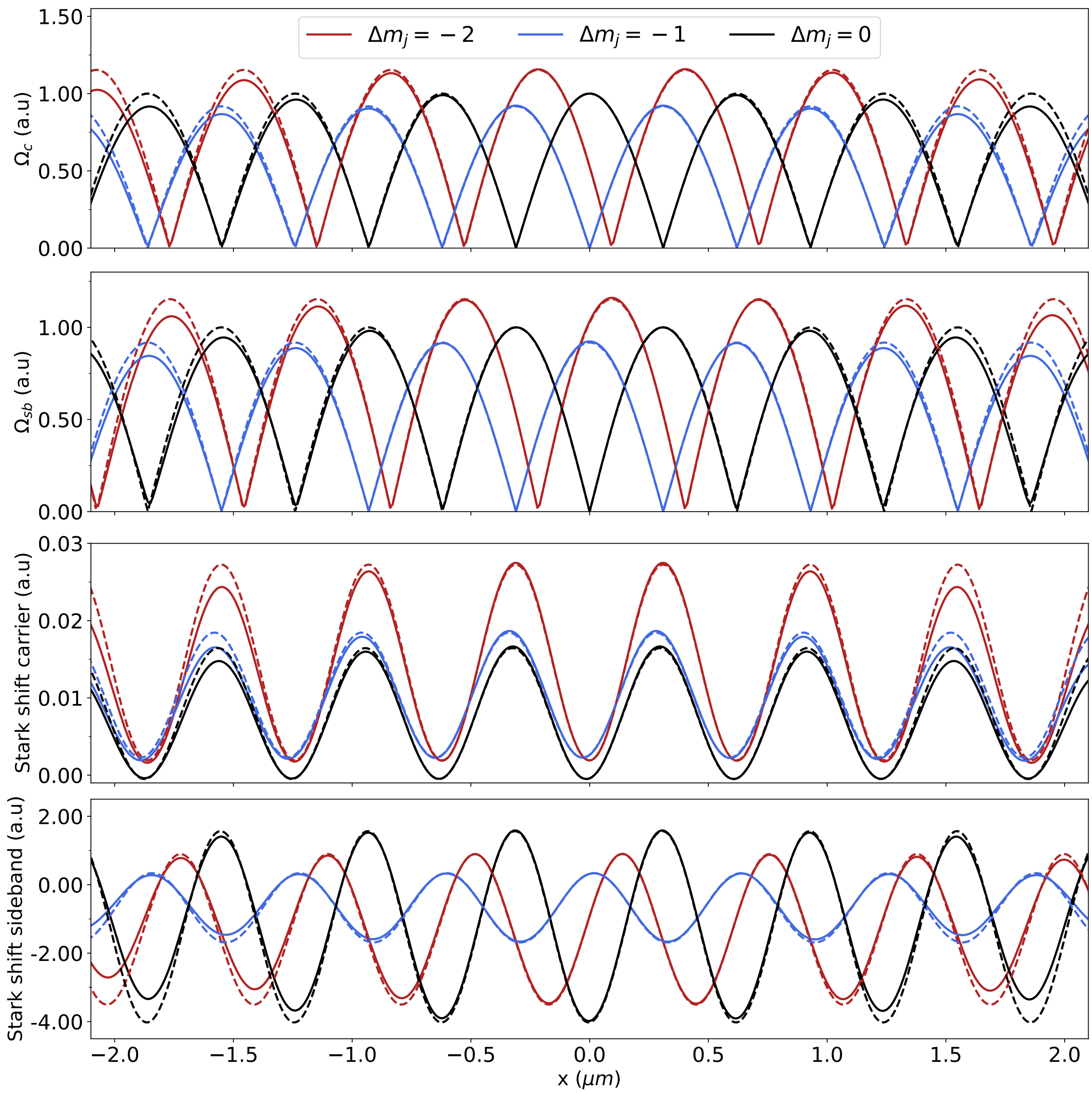

Figure 4.6: Carrier (*first*) and sideband *second*) Rabi frequencies and carrier (*third*) and sideband (*fourth*) AC Stark shifts.

and sideband Rabi frequencies and between the different transitions, the Stark shifts also provide important insigths. The carrier Stark shift, highly dominated by dipole contributions, is nearly in phase for all the three transitions and oscillates with the standing wave. The $\Delta m_j = 0$ transition Stark shift has a minimum that is negative, the other two remain positive. Minimizing the AC Stark shift in a carrier optical transition might be relevant for high accuracy frequency measurements for optical clocks for instance and is there provided by the standing wave pattern itself.

If we now consider the sideband Stark shifts for the three transitions, they are not in phase anymore since the quadrupole contribution from the closest carrier is now taken into account and thus at the origin of this dephasing. On top of that, they all reach zero twice per wavelength, which is again an advantage for calibration. We can for instance drive the blue sideband $|4S_{1/2}, m_j = -1/2\rangle \rightarrow |3D_{5/2}, m_j = -5/2\rangle$ transition at positions where there is no AC Stark shift. Regarding calibration, the sideband Stark shift has the same order of magnitude as the sideband Rabi frequency, it is therefore important to calibrate it with high accuracy in order to be able to actually drive the sideband.

4.2 Variations

4.2.1 Influence of the magnetic field

Orientation in the trap plane

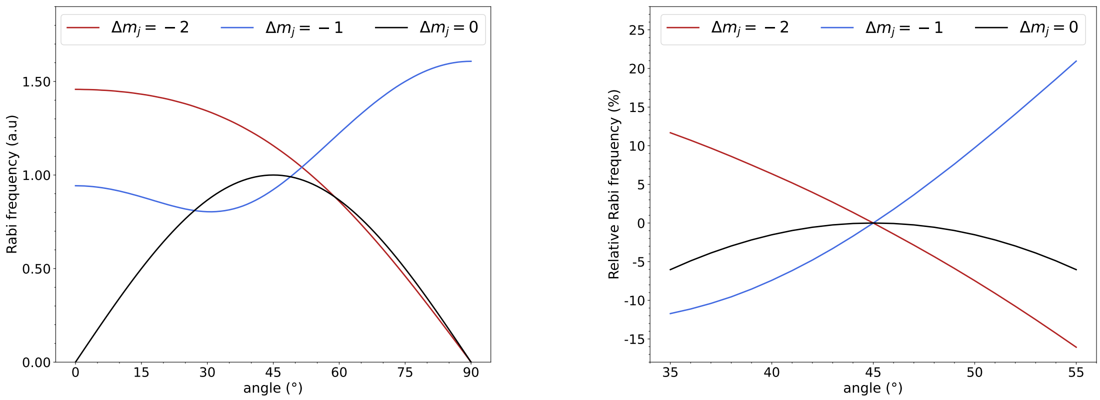

Figure 4.7: Influence of the in-plane angle θ. Maximum values of the Rabi frequencies as a function of the angle of the magnetic field in the $x - y$ plane, normalised by the value of the transition with $|\Delta m_j| = 0$ at 45° (*left*). Zoom around the theoritical value of $\theta = 45°$ (*right*), where all each transition's values are relative to their value at $\theta = 45°$.

One degree of freedom of the set-up lies into the orientation of the magnetic field. It is in the $x - y$ trap plane with a $\theta = 45°$ angle to the x axis. However, by varying this angle, we can engineer the maximum and minimum values of the Rabi frequencies. For instance, let us study what happens *around* the center of the trap at position $x = 0, y = 0$. For that I consider the fringe of each Rabi frequency transitions $|4S_{1/2}, m_j = -1/2\rangle$ to $|3D_{5/2}, m_j = -5/2, -3/2 \text{ and } -1/2\rangle$ that is the closest to the trap center and study how the maximum values of these fringes evolve with the magnetic field angle θ in the trap plane. As we can see in Figure 4.7 a small difference in the angle θ can make a great difference in the magnitude of the Rabi frequency. As expected, transitions with the same $|\Delta m_j|$ behave the same way: $|\Delta m_j| = 2$ are decreasing with θ whereas $|\Delta m_j| = 1$ are increasing with it; $|\Delta m_j| = 0$ behaves as a parabola of negative curvature centered at $\theta = 45°$. Around this value, the maximum of the transition with $\Delta m_j = 0$ is maximum with respect to θ and has thus a small gradient with respect to this variable. Whereas transitions with $|\Delta m_j| = 2$ and $|\Delta m_j| = 1$ have a strong gradient with respect to θ and thus can significantly vary with it. As pictured in Figure 4.7, in between $\theta = 40°$ and $\theta = 50°$, they respectively vary of approximatively of 27% and 35% of their value at $\theta = 45°$. Thus, any stray magnetic field that would change the angle of the magnetic field would also significantly change the Rabi frequencies of those two transitions. On top of that, working at $\theta = 45°$ seems to be good tradeoff to have as high Rabi frequencies as possible. And noticeably, some angle values yield same magnitude of Rabi frequency maximum for two transitions as for instance at $\theta = 60°$ for the transitions with $|\Delta m_j| = 0$ and 1. Nevertheless an error in the orientation of the magnetic field is only expected to be a few degrees such that this should not actually happen.

Angle out of the trap plane

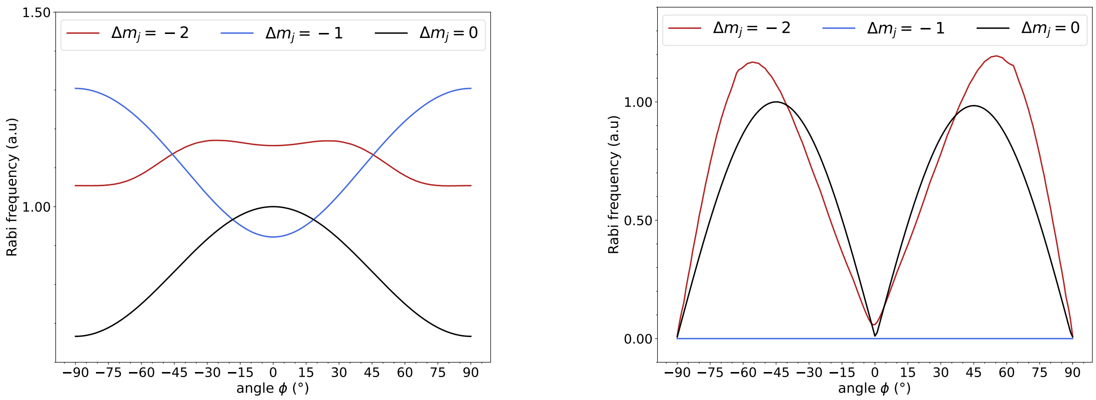

Figure 4.8: Influence of the out of trap plane angle ϕ. Maximum (*left*) and minimum (*right*) values of the Rabi frequencies as a function of the angle of the magnetic field out of the $x - y$ plane. The maximum (resp. minimum) values are normalised with respect to the value at $\phi = 0$ (resp. $\phi = 55$) of the $|\Delta m_j| = 0$ transition.

If we now do the same study but considering that the magnetic field makes an angle ϕ with the $x - y$ plane. In that case, not only the maximum values but also the minimum values of the transitions are affected such that the contrast tends to decrease. Here again in Figure 4.8, transitions with same absolute Δm_j show the same general behavior: maximum values of transitions with $|\Delta m_j| = 2$ do not vary significantly with ϕ - less than 10% -, whereas transitions with $|\Delta m_j| = 1$ are minimum at $\phi = 0$ and vary of 40% over the angle span. The transition with $|\Delta m_j|$ =0 varies also by 30% but is maximum at $\phi = 0$. Thus all transitions have a local extremum at $\phi = 0$, which makes their maximum values of Rabi frequency little sensitive to an out-of-plane stray field. Unfortunately,the minimum values of the Rabi frequencies are dependent on ϕ (see Figure 4.8), except for the transitions with $|\Delta m_j|$ =1 whose minimum values remain 0, hence preserving good extinction. On the contrary, all the other transitions have a minimum value of 0 at $\phi = 0$ that increase symmetrically to

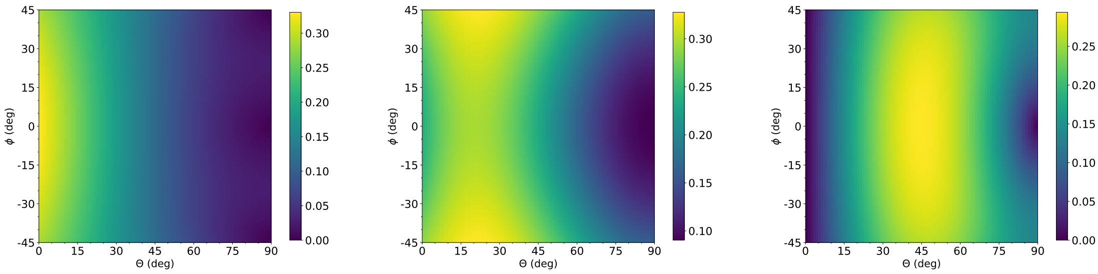

Figure 4.9: Coupling as a function of the magnetic field angles θ and ϕ for transitions with $\Delta\ m_j = -2$ (*left*), $\Delta\ m_j = -1$ (*center*) and $\Delta\ m_j = 0$ (*right*).

$\phi = 0$ with strong gradients that hinder perfect extinction of these Rabi frequencies. This nice feature provided by the standing wave could then be lost, if there is any stray field out of the trap plane.

Coupling strenghts as a function of the angles of the magnetic field

In Figure 4.9 I plotted the couplings as a function of the angles θ and ϕ of the magnetic field. Indeed, as we have seen in the previous section, the maximum possible values of the Rabi frequencies are dependent on both angles. The coupling, defined as $g(\Delta m_j, \theta, \phi) = \left| -c_{y,x}^{(\Delta m_j)} \sin(36°) + i c_{y,z}^{(\Delta m_j)} \cos(36°) \right|$ where all the dependence on θ and ϕ is hidden in $c_{i,j}^{(\Delta m_j)}$ which is rotated according to the magnetic field direction. Here, for the three considered values of Δm_j, the orientation of the magnetic field in the $x - y$ plane mainly governs the the values of the couplings. Sitting at $\theta = 45°$, $\phi = 0°$ is a trade-off to have good couplings values in the three transitions.

4.2.2 If the laser light were an ideal plane wave

Ideally, the laser light should be the sum of two counter-propagating plane waves and be only y-polarised. However, the finite-difference time-domain simulation of the electric field provided by K. Mehta shows that it is not the case when the ion is away from the trap axis $y = 0$. As we can see in Figure 4.6, the discrepencies with the plane wave are particularly important away from the trap center $x = 0$. The *real* light is indeed foccussed there and has a Gaussian shape. Thus, both the Rabi frequencies and the Stark shift amplitudes are decreasing when the ion moves away from the trap center. Experimentally, this is something we notice when measuring the Stark shifts: different amplitudes of Stark shift in two measurements, which was at first a bit puzzling, before realising that it is indeed to be expected.

4.2.3 Defects

The standing wave is constituted by interfering light coming from two couplers. It might happen that they are misplaced, for instance more spaced than expected. Let us suppose the right coupler is x_o farther away from the left coupler than supposed to be. The electric field reads

$$\vec{E} = \left(E_o e^{i\phi} e^{ik_z z} e^{-ik_x x} + E_o e^{i\phi} e^{ik_z z} e^{ik_x (x+x_o)} \right) \vec{\epsilon}$$

$$\vec{E} = 2E_o e^{i\phi} e^{ik_z z} e^{-ik_x x_o/2} \cos(k_x x + k_x x_o/2) \vec{\epsilon}$$

There is a global phase that depends on the displacement and a dephasing in the cosine. Other than that, nothing changes.

4.3 Light with orbital angular momentum

This paragraph aims at linking properties of the standing wave to more general properties of electric fields [30],[31].

4.3.1 Light with OAM

Photons also are particules with spin, they have a spin $S = 1$, and it is also possible to associate an OAM. The latter is related to the spatial distribution of the field, not to its polarisation. Let us consider a decomposition of the light in Laguerre-Gaussian modes $u_{l,p}$ with $p \in \mathbb{N}$ the radial index, $l \in \mathbb{Z}$ the azimuthal, $\mathcal{L}_p^{|l|}$ generalized Laguerre polynomial index [24]

$$u_{p,l}(r,\phi,z) = \sqrt{\frac{2p!}{\pi(p+|l|)}} \frac{w_o}{w(z)} \left(\frac{r\sqrt{2}}{w(z)} \right)^{|l|} \exp\left(-\frac{r^2}{w(z)^2} \right) \mathcal{L}_p^{|l|} \left(\frac{2r^2}{w(z)^2} \right)$$
$$\times \exp\left(-ik\frac{r^2}{2R(z)} \right) \exp(-il\phi) \exp(i\Psi(z)).$$

R(z) is the wavefront curvature, $\Psi(z)$ the Gouy phase and $w(z)$ the radius of the beam. The factor $\exp(-i|l|\phi)$ advances or retardes the phase by an integer multiple of 2π for each phase ϕ: the wavefront has thus a helicoidal shape for $l \neq 0$ which conveys a momentum. When the Rabi frequencies are derived, Wigner-3j symbols are involved. They not only ensure and dictate that the conservation rules are observed, but also their value gives weight to the momentum transfer.

4.3.2 The importance of strong field gradients

As we have seen, the standing wave pattern allows to drive electronic transitions where the light intensity is zero due to the strong spatial gradients. A finite-difference time-domain simulation, done by Gillen Beck [2], of Laguerre mode 1 of a 732nm laser that drives the $4S_{1/2}$ to $3D_{3/2}$ transition, is an illustration of it. In Figure 4.10, we observe that the Rabi frequencies follow the beam shape pattern. Transitions with $|\Delta m_j| = 1$ can hardly never be driven due to small Rabi frequencies, even in the position of no light intensity at the center of the beam. Indeed, the beam spot is large, $\approx 10\mu$m, thus gradients along the x axis for instance are small and cannot participate in driving transitions.

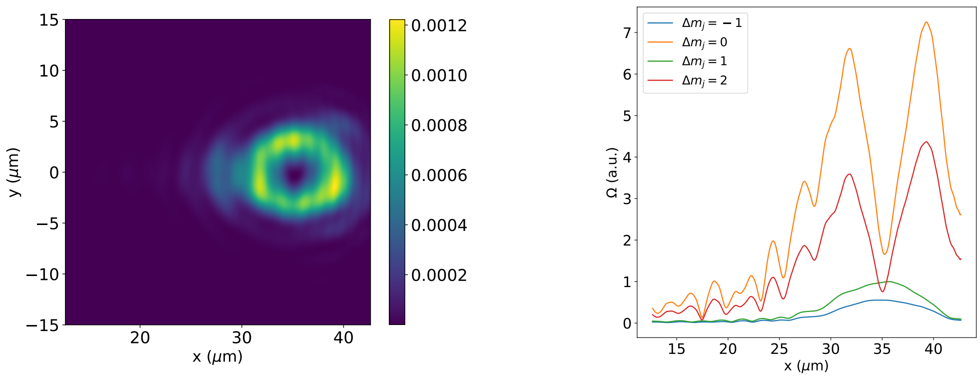

Figure 4.10: *Left*: intensity of a LG mode 1 at 732nm with waist $wo = 2\mu$m. *Right*: Rabi frequencies for the $|4S_{1/2}, m_j = -1/2\rangle$ to all sublevels $|3D_3/2, m_j = -3/2, -1/2, 1/2, 3/2\rangle$ when driving the transitions with this electric field.

4.4 Comparison with experimental data

In Figure 4.11, I show the Rabi frequencies and Stark shift of the carrier and sideband transitions extracted from data taken on the 13/12/2021 by Alfredo Ricci Vasquez and Carmelo Mordini (see first and second rows of the figure) and those from simulation (see third and fourth row of the figure). The theoritical simulation results match the experimental data quite good.

[2]Ph.D. student in the TIQI group.

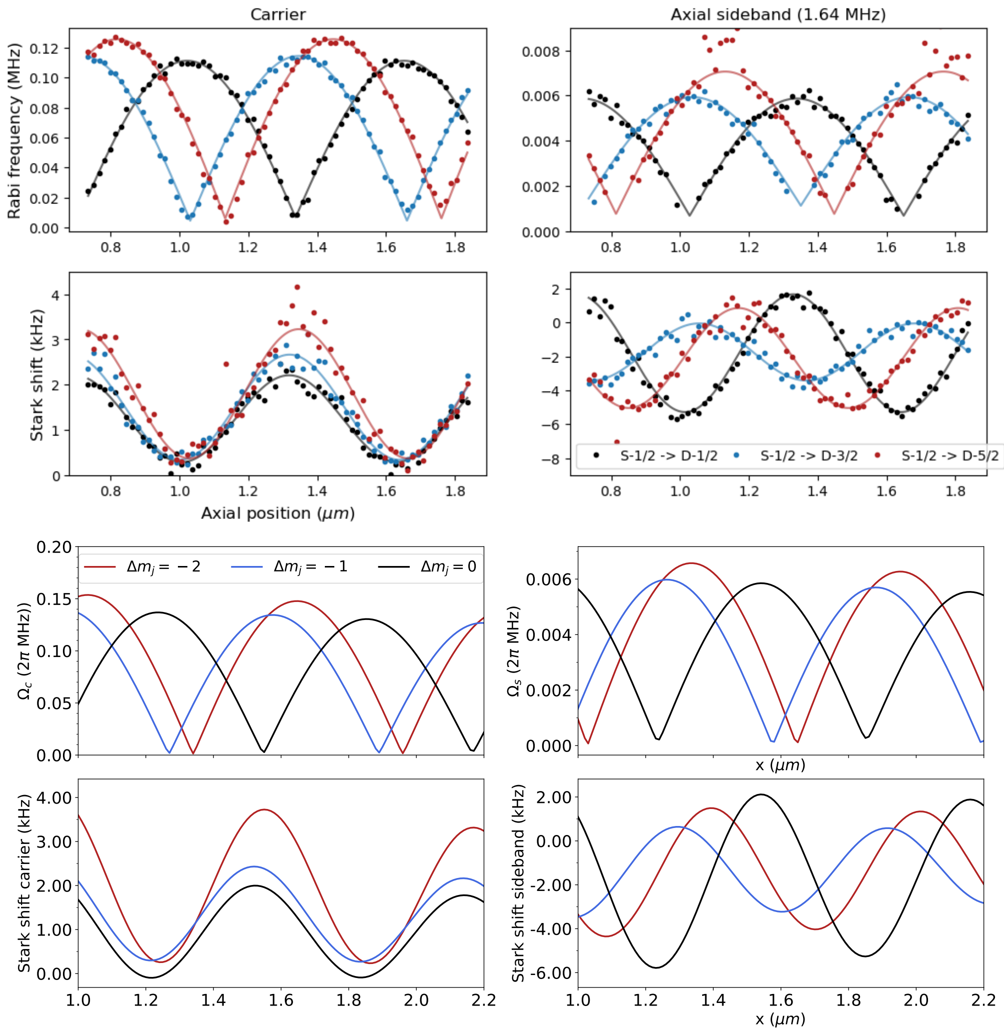

Figure 4.11: Experimental results from 13.12.2021 : carrier Rabi frequencies (*first row left*) and Stark shift (*second row left*) and sideband Rabi frequencies (*first row right*) and Stark shift (*second row right*). Dots are data points and full line a sinusoidal fit. The theoritical simulation results (*third and fourth rows*) follow the same layout.

Chapter 5

Motional effects on the Rabi frequency

One should consider that the Rabi frequency also depends on the average vibrational occupancy number $\bar{n}_m$ for each motional mode m. We actually only need to take into account motion along the axis of the trap as it is along the standing wave, which shows strong dependency on the axial position, reason why the radial modes along y and z have then little impact.

5.1 Temperature measurements

To deal with that, let us write the state of the ion as

$$|\Psi(t)\rangle = \sum_{n=0}^{\infty} p_n |\phi(t)\rangle |n\rangle$$

where $|\phi(t)\rangle$ is the state of the qubit at time t and $(p_n)_n$ the probability to have n quanta of motion in the motional state. The probility P to be in the $|1\rangle$ state is then given by

$$P(t) = Tr(|\Psi(t)\rangle \langle\Psi(t)|1\rangle \langle 1|)$$

$$P(t) = \frac{1}{2}\left(1 + \sum_n p_n \cos(\Omega_n t)\right) \tag{5.1}$$

with $\Omega_n = \Omega \langle n| \cos(k_x \hat{x}) |n\rangle$ is the Rabi frequency for each mode occupation number. Here Ω is the carrier Rabi frequency at the position of the ion This is different from the probability we get without considering motion

$$\mathcal{P}(t) = \frac{1}{2}\left(1 + \cos(\Omega t)\right). \tag{5.2}$$

Supposing the distribution of the motional modes is a thermal distribution $p_n = \frac{1}{\bar{n}+1}(\frac{\bar{n}}{\bar{n}+1})^n$ [22] we can fit the Rabi flop so as to extract $\bar{n}$ and Ω. What we actually is to first measure the average occupation motional number $\bar{n}$, which is proportional to temperature, by doing sideband flopping before fitting Ω in Equation (5.1).

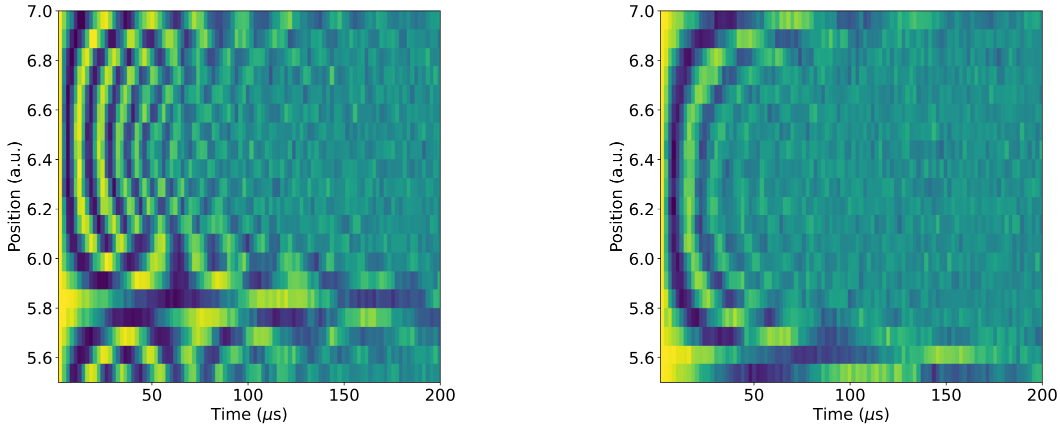

Figure 5.1: Rabi flops as a function of position with waiting time of 0ms (*left*) and 10ms (*right*).

To see the influence of the motion and temperature on the Rabi frequencies, we perform Rabi flopping as a function of position along the x axis[1]. We repeat these measurements with different values of waiting time $\Delta t_{wait} = 0; 1; 2; 5; 10$ms after Doppler cooling and state preparation so that the ion can heat up. Each experiment consists in: preparing the qubit in $|0\rangle$ through spin-polarisation; waiting during Δt_{wait}; driving the transition with 729nm laser; reading out the state; repeating this procedure 100 times to get statistics. In Figure 5.1 are presented the Rabi flops performed for 0ms and 10ms of waiting time respectively as a function of position: the decoherence due to heating caused by the waiting time is clearing to be seen in the lost of constrast.

To measure the temperature for all the waiting times, we independently do Rabi flopping on the red and blue sidebands. Knowing the expected value of $\bar{n}$ for each waiting time then allows to extract only the carrier Rabi frequencies from the Rabi flops following Equation (5.1). Sitting at a position where the sideband Rabi frequency is maximum, *i.e.* the carrier Rabi frequency is minimum, the relation $\Omega_c = \eta\Omega_s$ holds. Fitting the blue and red sideband flops respectively is then straightforward with [22]

$$P_{\bar{n}}^{bsb}(t) = s + (1-s)\sum_n \left(\frac{\bar{n}}{\bar{n}+1}\right)^n \cos\Big(\eta\sqrt{n+1}\Omega_c t\Big);$$

$$P_{\bar{n}}^{rsb}(t) = s + (1-s)\sum_n \left(\frac{\bar{n}}{\bar{n}+1}\right)^n \cos\big(\eta\sqrt{n}\Omega_c t\big)$$

where theoritically $s = 1/2$. However, due to poor spin-polarisation, the flops tend to an asymptotic value which is higher than 0.5 (see Figure 5.2), that is why I also let the spin-polarisation as a free parameter s.

[1] Due to experimental constraints, no EIT cooling was performed during the whole experiment.

Waiting time (ms)	BSB	RSB
0	(7.5 ± 0.3)	(5.9 ± 0.3)
1	(9.0 ± 0.4)	(10.2 ± 0.5)
2	(12.8 ± 0.6)	(12.1 ± 0.6)
5	(20.2 ± 1.1)	(19.0 ± 1.1)
10	(33.8 ± 2.4)	(38.5 ± 2.8)

Table 5.1: Summary of the extracted values of $\bar{n}$ for the blue sideband (BSB) and red sideband (RSB) for each of the waiting times.

We have a reliable estimate of Ω by fitting the Rabi flop with Equation (5.2) at a position where the carrier Rabi frequency is maximum. We extract $\Omega = 0.136 \times 2\pi$MHz from the data presented in Figure 5.2.

Fitting both sidebands gives us two estimates for $\bar{n}$ at each waiting time, see Figure 5.2) and Table 5.1.

According to former measurements [32] done on the trap by Maciej Malinkowski during his Ph.D. thesis, with an axial frequency of 1.53MHz, we can expect a heating rate of roughly 2 quanta/ms. Here it is 2.7q/ms for the RSB and 3.11q/ms for the BSB. Despite this difference, values for both the blue and red sidebands agree within error bars. The initial value, without any waiting time, after Doppler cooling but before EIT cooling, was measured during Maciej's thesis to be $\bar{n} \approx 8$ quanta (for an axial frequency of 1.3 MHz), which does not contradict the results here presented.

5.2 Influence of the temperature on the Rabi frequencies

Using the average of these values of $\bar{n}$ for each of the waiting times, I can now fit the Rabi frequency Ω of the Rabi flops with Equation (5.1) - I call this Method 1. Results are presented in Figure 5.3 where I plot the Rabi frequencies as a function of position for the different waiting times. We can recognize the particular pattern due to the standing wave. However, we notice that the ion drifts along the x axis as function of the waiting time, with a saturation value of 0.2"μm". Since the standing wave is phase-stable, it is indeed the ion and the pattern that drifts. This could then be due to the presence of stray fields. This also confirms the fact that what is named "position (μm)" is actually only an estimate for it. To know the real position, one has to use the standing wave pattern, since it is stable. Using its periodicity, I plot the Rabi frequency values in the right panel with a recalibration of the distance.

As a function of the waiting time, we see that the values for the Rabi frequency decrease. This behavior is particularly marked where the Rabi frequency is maximum and seems also to saturate with the waiting time.

However, the extracted values obtained by this method - Method 1 - do not fit the Rabi flops very accurately. For comparison, I extract the value of $\bar{n}$ using the already-extracted value of Ω in (5.1) - I name this Method 2 - and in a third way also

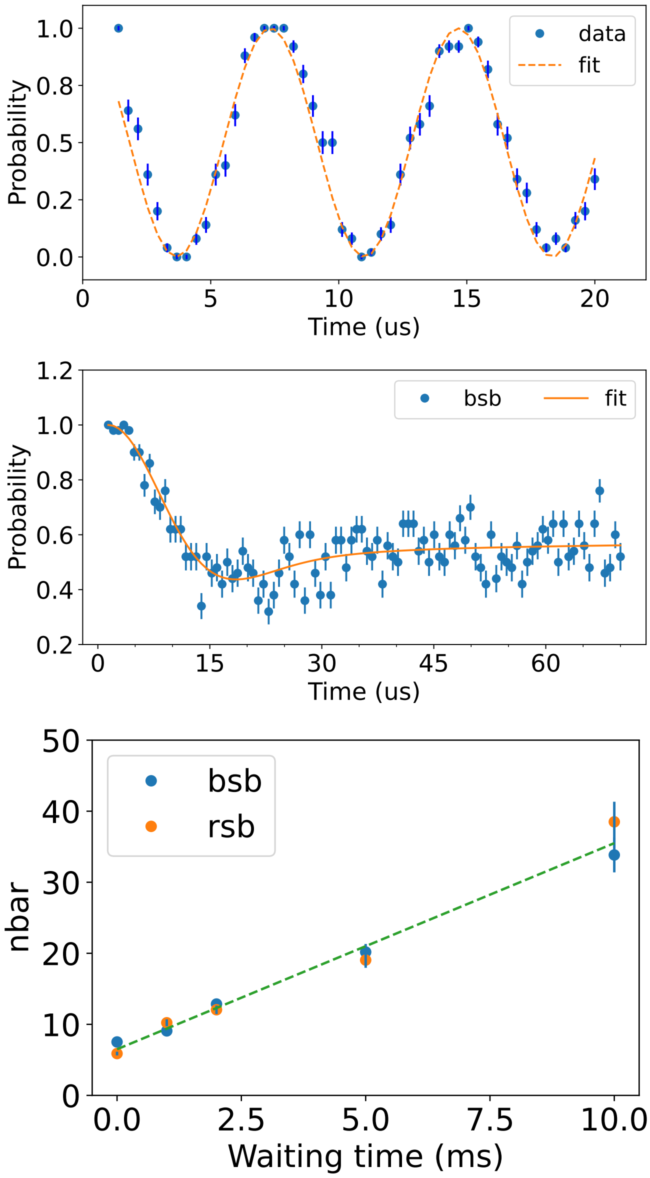

Figure 5.2: Results for the estimation of $\bar{n}$. *Top*: Rabi flop data (*blue dots*) and fit (*orange, dashed*). *Middle*: blue sideband flop after 10ms waiting time (*blue* data points) and fit (*orange*). *Bottom*: values of $\bar{n}$ given by both sideband fitting leaving spin-polarisation as a free parameter: blue sideband; *orange*: red sideband; *blue* : *dashed* : expected [32] evolution.

extract both the values of $\bar{n}$ and Ω in Equation (5.1) - I name this Method 3. As we can see in Figure 5.4 (*left*), the values for $\bar{n}$ differ by one order of magnitude between Method 1 and Methods 2 and 3. They nevertheless show a similar heating rate of approximatively 3 quanta/ms.

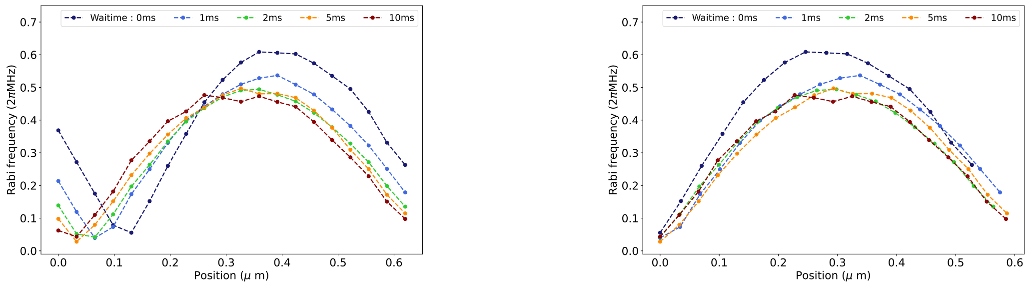

Figure 5.3: *Left*: extrated Rabi frequencies as a function of position and waiting time. *Right*: same values, with a recalibration of the position.

Despite these discrepancies, the optimal parameters given by Method 3 happen to fit decently the data. The extracted values for the Rabi frequency obtained with this method are presented in Figure 5.4, right panel. Even if the values reach higher values by $5-10\%$ than those of Method 1, they present the same behavior: decrease of the maximum Rabi frequency with temperature and saturation.

Due to random shot to shot variation in the position, we could have expected that at position with high Rabi frequency gradients the Rabi frequency would show a different behavior with temperature as compared with positions with no Rabi frequency gradient. There is no evidence for such an effect in the data I have presented here. Such that overall, we cannot say that there is a position-dependent temperature effect on the Rabi frequencies, but rather only a temperature one that is global over all the positions along the standing-wave pattern and that saturates quickly.

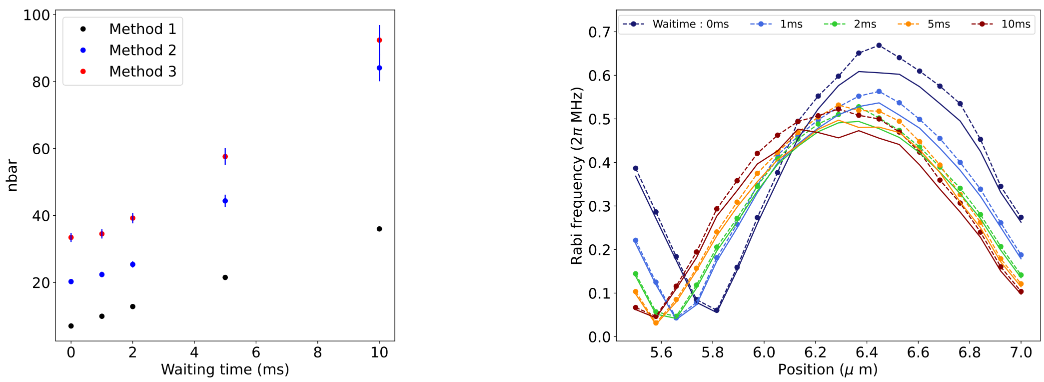

Figure 5.4: *Left*: values extracted for $\bar{n}$ with Methods 1,2 and 3. *Right*: values extracted for the Rabi frequencies with Method 1 (*full*) and Method 3 (*dashed*).

Chapter 6

Conclusion

The standing-wave pattern confers some of its properties to the ion, given the fact that quadrupole transitions are driven by spatial gradients. The tight foccussing of the beam as well as the phase stability ensured by the integrated photonics play here an important role in this property transfer. It follows that Rabi frequencies and consequently the total AC Stark shift values show oscillations in space. The values of the Rabi frequencies periodically reaches zero along the trap axis, which means that at those positions no transition can theoretically be driven. The orientation of the magnetic field and the coupling properties of the light with the transitions between $|4S_{1/2}\rangle$ and $|3D_{5/2}\rangle$ with $|\Delta m_j| = 0, 1$ or 2 governs the dephasing between the Rabi frequencies of those three transitions and their amplitudes. It is then possible not only to drive a transition with $|\Delta m_j| = 0$ at positions where theoretically a transition with $|\Delta m_j| = 1$ cannot be driven, such that off-resonnant driving can be avoided, but more importantly to drive a sideband transition without coupling to the carrier one, since the carrier and sideband Rabi frequency for the same transition are out-of-phase. Finally, the study of the influence of temperature on the Rabi frequency shows an attenuation of their maximum value and a fast saturation of this process.

The goal is now to capitalize on this property to implement a fast two-ion Mølmer-Sørensen gate with reduced error do to off-resonantly coupling to the carrier. One could also think of implementing a light-shift gate, due to the fact that the AC Stark shifts are also calculated and spatially varying. However, the dephasing one would need to run it are not straightforwardly implementable, and the gate time would never be as fast as the one a MS gate would give. On top of that, as already pointed out, the set-up provides natural reduction of some intrinsic source of error of a MS gate. First step towards the latter is the ability to load two ions in the trap and transport them in different trapping zones.

Other exploration possibilities can be found in the study of friction generated by the standing wave pattern, the variation of the magnetic field or the realisation of precise Laguerre-Gaussian modes of the light.

Appendix A

Appendix

A.1 Normalized spherical basis vectors

Given by [21], the normalized spherical basis vectors are

$$c^{(1)} = -\frac{1}{\sqrt{2}}(1, -i, 0);$$

$$c^{(0)} = (0, 0, 1);$$

$$c^{(-1)} = -\frac{1}{\sqrt{2}}(1, -i, 0);$$

$$c_{ij}^{(2)} = \frac{1}{\sqrt{6}} \begin{pmatrix} 1 & -i & 0 \\ -i & -1 & 0 \\ 0 & 0 & 0 \end{pmatrix};$$

$$c_{ij}^{(1)} = \frac{1}{\sqrt{6}} \begin{pmatrix} 0 & 0 & -1 \\ 0 & 0 & i \\ -1 & i & 0 \end{pmatrix};$$

$$c_{ij}^{(0)} = \frac{1}{3} \begin{pmatrix} -1 & 0 & 0 \\ 0 & -1 & 0 \\ 0 & 0 & 2 \end{pmatrix};$$

$$c_{ij}^{(-1)} = \frac{1}{\sqrt{6}} \begin{pmatrix} 0 & 0 & 1 \\ 0 & 0 & i \\ 1 & i & 0 \end{pmatrix};$$

$$c_{ij}^{(-2)} = \frac{1}{\sqrt{6}} \begin{pmatrix} 1 & i & 0 \\ i & -1 & 0 \\ 0 & 0 & 0 \end{pmatrix};$$

A.1.1 Wigner-Eckart theorem

Let $T^{(k)}$ be a tensor operator of rank k. Then, for all angular momenta j and j', there exists a constant $\langle j| |T^{(k)}| |j'\rangle$ such that for all m, m' and q [33]

$$\langle j, m| T_q^{(k)} |j', m'\rangle = \langle j'm'kq|jm\rangle \langle j| |T^{(k)}| |j'\rangle$$

where $T_q^{(k)}$ is the q^{th} component of the tensor operator $T^{(k)}$. $\langle j| |T^{(k)}| |j'\rangle$ is the reduced matrix element and is independent of m, m' and q.

A.2 Wigner-3j symbol and Clebsch-Gordon coefficients

Wigner-3j symbols $\begin{pmatrix} j_1 & j_2 & j_3 \\ m_1 & m_2 & m_3 \end{pmatrix}$ are 0 unless all the following conditions are satisfied [33]:

- $m_i \in [|-j_i, j_i|]$ for $i = 1, 2, 3$ (magnetic quantum number condition);
- $m_1 + m_2 + m_3 = 0$;
- $|j_1 - j_2| < j_3 < j_1 + j_2$ (conservation of the total angular momentum);
- $j_1 + j_2 + j_3 \in \mathbb{N}$.

They relate to the Clebsch-Gordan coefficients with

$$\begin{pmatrix} j_1 & j_2 & j_3 \\ m_1 & m_2 & m_3 \end{pmatrix} = \frac{(-1)^{(j_1 - j_2 - m_3)}}{\sqrt{2j_3 + 1}} \langle j_1 m_1 j_2 m_2 | j_3 - m_3\rangle .$$

And have the following orthogonality relation

$$\sum_{m_1, m_2} \begin{pmatrix} j_1 & j_2 & j_3 \\ m_1 & m_2 & m_3 \end{pmatrix} \begin{pmatrix} j_1 & j_2 & j_3' \\ m_1 & m_2 & m_3' \end{pmatrix} = \frac{1}{2j_3 + 1} \delta_{j_3, j_3'} \delta_{m_3, m_3'} \{j_1 j_2 j_3\}.$$

A.3 Relations to Einstein coefficients

Einstein A coefficients describe the rate for spontaneous decay from the excited state $|e\rangle$ to all the sublevels of the ground state $|g\rangle$ and we have for a dipole transition [21]

$$A_{eg}^{(E1)} = \sum_{m=-j}^{j} \frac{4c\alpha k_{eg}^3}{3} \sum_{q=-1}^{1} \left| \langle e| R_q^{(1)} |g\rangle \right|^2.$$

Applying the Wigner-Eckart theorem to the matrix element,

$$A_{eg}^{(E1)} = \sum_{m_j=-j}^{j} \frac{4c\alpha k_{eg}^3}{3} \left| \langle e| |R^{(1)}| |g\rangle \right|^2 \sum_{q=-1}^{1} \begin{pmatrix} j & 1 & j' \\ -m_j & q & m_j' \end{pmatrix}^2$$

and orthogonality relations of Wigner-3j symbol

$$A_{eg}^{(E1)} = \frac{4c\alpha k_{eg}^3}{3(2j'+1)}\left|\langle e|\,|R^{(1)}|\,|g\rangle\right|^2.$$

Analogously for a quadrupole transition we get

$$A_{eg}^{(E2)} = \frac{4c\alpha k_{eg}^5}{15(2j'+1)}\left|\langle e|\,|R^{(2)}|\,|g\rangle\right|^2.$$

A.4 Laguerre-Gauss decomposition and derivation of the Rabi frequency

The motivation for this section from discussions with Chi Zhang [1], who studied the Rabi frequencies with a plane wave decomposed in Laguerre-Gaussian modes, and from the lecture of [34]. I studied [33] to derive the following calculations.

Let us suppose we are working close to the beam center and decompose the laser light E over the Laguerre-Gauss modes LG_l^p

$$E = \sum_{p,l} \alpha_{p,l} LG_l^p$$

where $p \in \mathbb{N}$ is the radial index and $l \in \mathbb{Z}$ the azimuthal index. l can be associated with the OAM of light in the considered mode p, l. We want to evaluate: $\langle f| - e\vec{r}\vec{E}\,|i\rangle$ where $|f\rangle$, $|i\rangle$ are the final and initial states. Let us work in the beam frame and evaluate the electric field in the direction of propagation z_b and in the plane perdicular to it

$$\vec{E}_{l,p=0,\perp} = \vec{\epsilon}\,\frac{E_o}{\sqrt{\pi|l|!}w_o}\left(\frac{\sqrt{2}r}{w_o}\right)^{|l|} e^{il\phi}e^{ikz},$$

$$E_{l,p=0,z} = -i(l\sigma - |l|)(1-\delta_{l,0})\frac{E_o}{\sqrt{\pi|l|!}w_o}\left(\frac{\sqrt{2}}{w_o k}\right)\left(\frac{\sqrt{2}r}{w_o}\right)^{|l|-1} e^{i(l+\sigma)\phi}e^{ikz}$$

where $\vec{\epsilon}$ is the polarisation vector, σ the polarisation, w_o the beam waist. Precisely, considering from now on $p = 0$, we get for the OAM $l = 0$ and $l = 1$

l=0:

$$\vec{E}_\perp = \vec{\epsilon}\,\frac{E_o}{\sqrt{\pi}w_o}e^{ikz} \approx \vec{\epsilon}\,\frac{E_o}{\sqrt{\pi}w_o}(1+ikz);$$

$$E_z = 0$$

[1] Former Ph.D. student in the TIQI group.

and the Hamiltonians

$$H_\perp = -e\vec{r}.\overrightarrow{E_\perp}$$

$$H_\perp = e\frac{E_o}{\sqrt{\pi}w_o} r\sigma T^1_\sigma \left(1 + ikr\sqrt{\frac{4\pi}{3}}T^1_0\right)$$

$$H_\perp = e\frac{E_o}{w_o}\sigma\sqrt{\frac{4}{3}}\left(rT^1_\sigma + ik\sqrt{\frac{2\pi}{3}}r^2\left(T^2_{-\sigma} + \sigma T^1_{-\sigma}\right)\right)$$

and $H_z = 0$.

Here T^n_m is the spherical harmonics tensor of order n and component m.

l=1:

$$\vec{E}_\perp = \vec{\epsilon}\frac{E_o}{\sqrt{\pi}w_o}\left(\frac{\sqrt{2}r}{w_o}\right)e^{i\phi}e^{ikz} \approx \vec{\epsilon}\frac{E_o}{\sqrt{\pi}w_o}\left(\frac{\sqrt{2}}{w_o}\right)re^{i\phi}(1 + ikz)$$

$$E_z = -i(\sigma - 1)\frac{E_o}{\sqrt{\pi}w_o}\left(\frac{\sqrt{2}}{w_o k}\right)e^{i(1+\sigma)\phi}e^{ikz} \approx -i(\sigma - 1)\frac{E_o}{\sqrt{\pi}w_o^2}\left(\frac{\sqrt{2}}{k}\right)e^{i(1+\sigma)\phi}(1 + ikz)$$

and the Hamiltonians

if $\sigma = 1$: $H_z = 0$ so

$$H = H_\perp = -e\frac{8}{3}\sqrt{2\pi}\frac{E_o}{w_o^2}\left(r^2T^2_2 + \frac{\sqrt{4\pi}}{3}ikr^3\left(T^3_2 + \sqrt{2}T^2_2\right)\right).$$

If $\sigma = -1$

$$\begin{aligned} H_\perp = e\frac{8}{3}\sqrt{2\pi}\frac{E_o}{w_o^2}&\left(r^2\left(\frac{1}{\sqrt{3}}T^0_0 - \frac{1}{\sqrt{2}}T^1_0 + \frac{1}{\sqrt{6}}T^2_0\right)\right. \\ &\left. + ik\sqrt{\frac{4\pi}{3}}r^3\left(-\frac{1}{\sqrt{3}}T^2_0 + \frac{1}{\sqrt{6}}T^0_0 + \frac{1}{\sqrt{10}}T^3_0 - \frac{1}{\sqrt{15}}T^1_0\right)\right) \end{aligned} \tag{A.1}$$

$$H_z = -i2e\sqrt{\frac{8}{3}}\frac{E_o}{w_o^2}\frac{1}{k}T^1_0 + e\frac{E_o}{w_o^2}\frac{8}{3}\sqrt{2\pi}r^2\left(\sqrt{\frac{2}{3}}T^2_0 - \frac{1}{\sqrt{3}}T^0_0\right).$$

Before adding the field from the second coupler, let us discard the terms that will be zero when considering the matrix element with $|i\rangle = |1/2, -1/2\rangle$ and $|f\rangle = |5/2, m'\rangle$. According to the Wigner-Eckart theorem, $\langle 1/2, 1/2|\, T^k_q\, |5/2, m'\rangle$ is proportionnal to the Clebsch-Gordan coefficient $\langle 5/2, m', kq|1/2, 1/2\rangle$ which is proportionnal to the Wigner-3j symbol $\begin{pmatrix} 5/2 & k & 1/2 \\ m' & q & -1/2 \end{pmatrix}$. For the latter not to be zero, we first need to have $k = 2$ or $k = 3$. Then $q = 1/2 - m'$ depends on the transition taken into account. Actually, T^3_0 will not contribute for the three transitions considered in this thesis such that only rank 2 tensors matter. This was expected, as the quadrupole transition involves up to 2 OAM quanta transfer.

We now add the rotated field from the second coupler and only take into account spherical harmonic tensors of rank 2 or 3. The rotation is performed with Euler angles $\alpha = 0$, $\beta = 112°$ and $\gamma = \pi$. The rotation is formalized by the Wigner-D matrix $D^j_{m'm}(\alpha, \beta, \gamma) = \langle jm' | R(\alpha, \beta, \gamma) | jm \rangle$ and $d^j_{m'm}(\beta) = D^j_{m'm}(0, \beta, 0)$. We get

l=0

$$H \propto e\frac{E_o}{w_o}\sigma\frac{\sqrt{8\pi}}{3}ikr^2[T^2_{-\sigma} + \sum_{q=-2}^{2} T^2_q d^{(2)}_{q-\sigma}(\beta)].$$

l=1

For $\sigma = 1$

$$H \propto -e\frac{E_o}{w_o^2}\sigma\frac{8}{3}\sqrt{2\pi}r^2[T^2_2 + \sum_{q=-2}^{2} T^2_q d^{(2)}_{q2}(\beta)].$$

For $\sigma = -1$

$$H \propto e\frac{E_o}{w_o^2}\sigma\frac{8}{3}\sqrt{2\pi}r^2\frac{3}{\sqrt{6}}[T^2_0 + \sum_{q=-2}^{2} T^2_q d^{(2)}_{02}(\beta)].$$

Finally we need to rotate the Hamiltionian to align the magnetic field and the z axis. To do so, we use the Euler angles $\alpha = \arctan\left(\sqrt{2}tan(36°)\right)$, $\beta = \arccos\left(\frac{\sqrt{2}}{2}\cos(36°)\right)$ and $\gamma = \arctan(1/\sin(36°))$. This finally yields

l=0

$$\begin{aligned} H \propto e\frac{E_o}{w_o}\sigma\frac{\sqrt{8\pi}}{3}ikr^2 \sum_{s'=-2}^{2} T^2_{s'}[D^2_{s',-\sigma}(\alpha,\beta,\gamma)(1 - d^2_{-\sigma,-\sigma}(112)) \\ - \sum_{q=-2, q\neq-\sigma}^{2} D^2_{s',q}(\alpha,\beta,\gamma)d^{(2)}_{q,-\sigma}(112)]. \end{aligned} \quad \text{(A.2)}$$

l=1

For $\sigma = 1$

$$H \propto -e\frac{E_o}{w_o^2}\sigma\frac{8}{3}\sqrt{2\pi}r^2 \sum_{s'=-2}^{2} T^2_{s'}[D^2_{s',2}(\alpha,\beta,\gamma)(1 - d^2_{2,2}(112)) - \sum_{q=-2}^{1} D^2_{s',q}(\alpha,\beta,\gamma)d^{(2)}_{q,2}(112)].$$

For $\sigma = -1$

$$H \propto e\frac{E_o}{w_o^2}\sigma\frac{8}{3}\sqrt{2\pi}r^2 \sum_{s'=-2}^{2} T_{s'}^2 [D_{s',0}^2(\alpha,\beta,\gamma)(1 - d_{0,0}^2(112)) - \sum_{q=-2,q\neq 0}^{2} D_{s',q}^2(\alpha,\beta,\gamma) d_{q,0}^{(2)}(112)]. \quad (A.3)$$

Evaluating those Hamiltonians for the transitions with $|\Delta m_j| = 0, 1, 2$ yields the same values as the Rabi frequencies I computed with the field simulation at position (x,y) = $(0, 0)$ in the trap.

A.5 Procedure for fitting the data

To fit data, I have used the function *curve$_f$it* from the *scipy.optimize* package of python which uses the Trust Region Reflective algorithm to find the optimal parameters. This function takes the following arguments:

- the model function to use for fitting;
- the data Y to be fitted;
- a starting point for the optimisation;
- the error ΔY on each data point.

I iterate the optimisation by using the previous optimisation parameters until they do not vary by more than 1% (if relevant).

The function gives the optimal parameters as well as the covariance matrix on them.

On top of that, I am sometimes supposed to fit over an infinite sum - blue sideband fitting for instance. However, to ease the computaional part, fitting over a sum until $n = 250$ is enough since it gets all the weight of the thermal probability distribution up to 0.1% in the worst case scenario of $\bar{n} = 40$.

A.6 Derivation of the thermal distribution Rabi flop at the maximum of light intensity

Before taking the straightforward approach presented in Chapter 5, I had studied the results from [35] which also studies how the motion affects the Rabi frequency of an ion. This approach is not the most direct one for the results I have and also makes strong hypothesis about the position of the ion in the beam. Nevertheless, as I had struggled to derive their results, I would like to write the derivation here.

Let us suppose the ion is in thermal equilibrium with an average axial occupancy number $\bar{n}$. The probability distribution of the occupation number n is given by

$$P(n) = \frac{1}{\bar{n}+1}(\frac{\bar{n}}{\bar{n}+1})^n.$$

The probability $\mathcal{P}_{\bar{n}}$ to find the qubit in $|1\rangle$ is then a thermal average given by

$$\mathcal{P}_{\bar{n}} =< \sin(\Omega t)^2 >;$$

$$\mathcal{P}_{\bar{n}} = \sum_{n=0}^{\infty} P(n)(\frac{1}{2} + \frac{\cos\left(\Omega_0 t + \Omega_0'' n t x_0^2 t\right)}{2});$$

$$\mathcal{P}_{\bar{n}} = \frac{1}{2} + \frac{e^{i\Omega_0 t}}{4}\sum_{n=0}^{\infty} P(n) e^{i\Omega_0'' n t x_0^2 t} + \frac{e^{-i\Omega_0 t}}{4}\sum_{n=0}^{\infty} P(n) e^{-i\Omega_0'' n x_0^2 t};$$

$$\mathcal{P}_{\bar{n}} = \frac{1}{2} + \frac{e^{i\Omega_0 t}}{4(\bar{n}+1)}\frac{1}{1-\frac{\bar{n}}{\bar{n}+1}e^{i\Omega_0'' x_0^2 t}} + \frac{e^{-i\Omega_0 t}}{4(\bar{n}+1)}\frac{1}{1-\frac{\bar{n}}{\bar{n}+1}e^{-i\Omega_0'' x_0^2 t}};$$

$$\mathcal{P}_{\bar{n}} = \frac{1}{2} + \frac{e^{i\Omega_0 t}}{4(\bar{n}+1)}\frac{1}{1-\frac{\bar{n}}{\bar{n}+1}e^{i\Omega_0'' x_0^2 t}} + \frac{e^{-i\Omega_0 t}}{4(\bar{n}+1)}\frac{1}{1-\frac{\bar{n}}{\bar{n}+1}e^{-i\Omega_0'' x_0^2 t}};$$

$$\mathcal{P}_{\bar{n}} = \frac{1}{2} + \frac{e^{i\Omega_0 t}}{4}\frac{1}{1+\bar{n}(1-e^{i\Omega_0'' x_0^2 t})} + \frac{e^{-i\Omega_0 t}}{4}\frac{1}{1+\bar{n}(1-e^{-i\Omega_0'' x_0^2 t})};$$

$$\mathcal{P}_{\bar{n}} = \frac{1}{2} + \frac{e^{i\Omega_0 t}}{4}\frac{1}{1-i\bar{n}\Omega_0'' x_0^2 t} + \frac{e^{-i\Omega_0 t}}{4}\frac{1}{1+i\bar{n}\Omega_0'' x_0^2 t};$$

and finally

$$\mathcal{P}_{\bar{n}} = \frac{1}{2} + \frac{1}{\sqrt{1+\bar{n}^2\Omega_0''^2 x_0^4 t^2}}\frac{cos\left(\Omega_0 t + \arctan\left(\bar{n}\Omega_0'' x_0^2 t\right)\right)}{2}.$$

Bibliography

[1] T. D. Ladd, F. Jelezko, R. Laflamme, Y. Nakamura, C. Monroe, and J. L. O'Brien. Quantum computers. *Nature*, 464:45–53, 3 2010.

[2] A fast quantum mechanical algorithm for database search. 5 1996.

[3] P.W. Shor. Algorithms for quantum computation: discrete logarithms and factoring. pages 124–134. IEEE Comput. Soc. Press.

[4] M. H. Devoret, A. Wallraff, and J. M. Martinis. Superconducting qubits: A short review. 11 2004.

[5] M. V. Gurudev Dutt, L. Childress, L. Jiang, E. Togan, J. Maze, F. Jelezko, A. S. Zibrov, P. R. Hemmer, and M. D. Lukin. Quantum register based on individual electronic and nuclear spin qubits in diamond. *Science*, 316:1312–1316, 6 2007.

[6] Colin D. Bruzewicz, John Chiaverini, Robert McConnell, and Jeremy M. Sage. Trapped-ion quantum computing: Progress and challenges. *Applied Physics Reviews*, 6:021314, 6 2019.

[7] H. Haeffner, C. F. Roos, and R. Blatt. Quantum computing with trapped ions. 9 2008.

[8] Wolfgang Paul. Electromagnetic traps for charged and neutral particles. *Rev. Mod. Phys.*, 62:531–540, Jul 1990.

[9] Daniel Gottesman, Alexei Kitaev, and John Preskill. Encoding a qubit in an oscillator. *Phys. Rev. A*, 64:012310, Jun 2001.

[10] K. A. Landsman, Y. Wu, P. H. Leung, D. Zhu, N. M. Linke, K. R. Brown, L. Duan, and C. Monroe. Two-qubit entangling gates within arbitrarily long chains of trapped ions. *Phys. Rev. A*, 100:022332, Aug 2019.

[11] J. M. Pino, J. M. Dreiling, C. Figgatt, J. P. Gaebler, S. A. Moses, M. S. Allman, C. H. Baldwin, M. Foss-Feig, D. Hayes, K. Mayer, C. Ryan-Anderson, and B. Neyenhuis. Demonstration of the trapped-ion quantum ccd computer architecture. *Nature*, 592:209–213, 4 2021.

[12] D. Kielpinski, C. Monroe, and D. J. Wineland. Architecture for a large-scale ion-trap quantum computer. *Nature*, 417:709–711, 6 2002.

[13] Karan K. Mehta, Chi Zhang, Maciej Malinowski, Thanh-Long Nguyen, Martin Stadler, and Jonathan P. Home. Integrated optical multi-ion quantum logic. *Nature*, 586:533–537, 10 2020.

[14] R. J. Niffenegger, J. Stuart, C. Sorace-Agaskar, D. Kharas, S. Bramhavar, C. D. Bruzewicz, W. Loh, R. T. Maxson, R. McConnell, D. Reens, G. N. West, J. M. Sage, and J. Chiaverini. Integrated multi-wavelength control of an ion qubit. *Nature*, 586:538–542, 10 2020.

[15] M. Ivory, W. J. Setzer, N. Karl, H. McGuinness, C. DeRose, M. Blain, D. Stick, M. Gehl, and L. P. Parazzoli. Integrated optical addressing of a trapped ytterbium ion. 11 2020.

[16] Thaned Pruttivarasin, Michael Ramm, Ishan Talukdar, Axel Kreuter, and Hartmut Häffner. Trapped ions in optical lattices for probing oscillator chain models. *New Journal of Physics*, 13:075012, 7 2011.

[17] I. García-Mata, O. V. Zhirov, and D. L. Shepelyansky. Frenkel-Kontorova model with cold trapped ions. *European Physical Journal D*, 41(2):325–330, sep 2007.

[18] Anders Sørensen and Klaus Mølmer. Entanglement and quantum computation with ions in thermal motion. *Physical Review A*, 62:022311, 7 2000.

[19] Karan Mehta, Chi Zhang, Stefanie Miller, and Jonathan P. Home. Towards fast and scalable trapped-ion quantum logic with integrated photonics. page 10. SPIE, 3 2019.

[20] D. J. Wineland, C. Monroe, W. M. Itano, D. Leibfried, B. E. King, and D. M. Meekhof. Experimental issues in coherent quantum-state manipulation of trapped atomic ions. 10 1997.

[21] D.F.V. James. Quantum dynamics of cold trapped ions with application to quantum computation. *Applied Physics B: Lasers and Optics*, 66:181–190, 2 1998.

[22] D. Leibfried, R. Blatt, C. Monroe, and D. Wineland. Quantum dynamics of single trapped ions. *Reviews of Modern Physics*, 75:281–324, 3 2003.

[23] J Chiaverini, R Reichle, John Bollinger, D Leibfried, J Britton, Janus Wesenberg, R.B. Blakestad, R.J. Epstein, D.B. Hume, Wayne Itano, J.D. Jost, Chris Langer,

R Ozeri, Nobuyasu Shiga, and D.J. Wineland. Microfabricated surface-electrode ion trap for scalable quantum information processing. *Physical review letters*, 96:253003, 07 2006.

[24] J. B. Götte and S. M. Barnett. *Light beams carrying orbital angular momentum*. Cambridge University Press, 2012.

[25] Chi Zhang. *Scalable Technologies for Surface-Electrode Ion Traps*. PhD thesis,ETH Zurich, 2021.

[26] S. Gulde, D. Rotter, P. Barton, F. Schmidt-Kaler, R. Blatt, and W. Hogervorst. Simple and efficient photo-ionization loading of ions for precision ion-trapping experiments. *Applied Physics B*, 73:861–863, 12 2001.

[27] H. Häffner, S. Gulde, M. Riebe, G. Lancaster, C. Becher, J. Eschner, F. Schmidt-Kaler, and R. Blatt. Precision measurement and compensation of optical stark shifts for an ion-trap quantum processor. *Physical Review Letters*, 90:143602, 4 2003.

[28] Regina Lechner, Christine Maier, Cornelius Hempel, Petar Jurcevic, Ben P. Lanyon, Thomas Monz, Michael Brownnutt, Rainer Blatt, and Christian F. Roos. Electromagnetically-induced-transparency ground-state cooling of long ion strings. *Physical Review A*, 93:053401, 5 2016.

[29] W. M. Itano, J. C. Bergquist, J. J. Bollinger, J. M. Gilligan, D. J. Heinzen, F. L. Moore, M. G. Raizen, and D. J. Wineland. Quantum projection noise: Population fluctuations in two-level systems. *Physical Review A*, 47:3554–3570, 5 1993.

[30] C. T. Schmiegelow and F. Schmidt-Kaler. Light with orbital angular momentum interacting with trapped ions. *European Physical Journal D*, 66, 2012.

[31] C.T. Schmiegelow, H. Kaufmann, T. Ruster, J. Schulz, V. Kaushal, M. Hettrich, F. Schmidt-Kaler, and U.G. Poschinger. Phase-stable free-space optical lattices for trapped ions. *Physical Review Letters*, 116:033002, 1 2016.

[32] Maciej Malinowski. *Unitary and Dissipative Trapped-Ion Entanglement Using Integrated Optics*. PhD thesis,ETH Zurich, 2021.

[33] A. N.; Khersonskii V. K. Varshalovich, D. A.; Moskalev. *Quantum Theory of Angular Momentum*. World Scientific Publishing Co., 1988.

[34] Christian T. Schmiegelow, Jonas Schulz, Henning Kaufmann, Thomas Ruster, Ulrich G. Poschinger, and Ferdinand Schmidt-Kaler. Transfer of optical orbital angular momentum to a bound electron. *Nature Communications*, 7:12998, 12 2016.

[35] M. Cetina, L. N. Egan, C. A. Noel, M. L. Goldman, A. R. Risinger, D. Zhu, D. Biswas, and C. Monroe. Quantum gates on individually-addressed atomic qubits subject to noisy transverse motion. 7 2020.